

High frequency attenuation of S-waves in alluvial deposits of the central Po Plain (northern Italy)

Gianlorenzo Franceschina¹ and Alberto Tento²

¹ *Istituto Nazionale di Geofisica e Vulcanologia, Sezione di Milano, Via Alfonso Corti 12, 20133 Milano, Italy.*
E-mail: gianlorenzo.franceschina@ingv.it

² *Retired, CNR - Istituto per la Dinamica dei Processi Ambientali, Milano, Italy.*

SUMMARY

Estimation of local seismic response plays a key role in assessing local seismic hazard and particularly in the design of shaking scenarios. Modeling local seismic response involves knowing of the shear wave velocity (V_S) and quality factor (Q_S) profiles for the site in question. The many techniques that have been developed to assess V_S in surface deposits produce reliable measurements of V_S , but these rarely correspond to direct measurements of Q_S . The latter is often considered through damping measures from laboratory tests on small-scale soil samples, which can provide information primarily on intrinsic attenuation, neglecting the contribution of scattering effects. In this paper, using seismic recordings obtained at the surface and in boreholes at 100 m depth, we estimate an average value of Q_S of some characteristic alluvial deposits of the Po Plain (northern Italy). Data come from a microseismic network which sampled an almost uniform lithology in the central Po Plain and consisted of three surface and four borehole stations with an inter-station distance of about 2 km. The average value of Q_S of the shallowest 100 m of the sedimentary strata, $Q_{S,100}$, is estimated by considering: (1) the high-frequency attenuation of seismic waves due to propagation through the corresponding stratigraphy and (2) the inter-

ference between incident and surface-reflected waves observed at borehole stations. We parameterize the first through $\Delta k_{0,100}$, the difference between the values of the spectral decay parameter kappa (k) estimated at the surface and at the boreholes depth, respectively. We use the second in order to compute $V_{S,100}$, the time-averaged V_S referred to the uppermost 100 m stratigraphy. We obtain: $\Delta k_{0,100} = (11 \pm 3)$ ms, $V_{S,100} = (309 \pm 11)$ m/s and $Q_{S,100} = 31 \pm 10$. At the surface, the estimated values of the site-specific kappa, k_0 , are found to range from 75 to 79 ms. As expected, these results are in good agreement with studies performed in other sites characterized by sandy or clayey lithologies, and can be usefully employed in site response analysis at sites where the rigidity is mainly controlled by lithostatic pressure.

Key words: Earthquake ground motions; Wave propagation; Wave scattering and diffraction; Seismic attenuation; Site effects.

1 INTRODUCTION

Near-surface attenuation of seismic waves is considered an important issue in both earthquake engineering and seismology. Many engineering applications need to consider seismic wave attenuation produced by sedimentary layers underlying the recording sites, and near-surface attenuation plays a key role in both deterministic and probabilistic seismic hazard assessment (Paolucci et al. 2014; Rodriguez-Marek et al. 2014). Ground motion simulation, as an example, must take into account the high frequency attenuation of seismic waves, in order to realistically constrain both peak and spectral shape ground motion (see Boore (2003) or Motazedian & Atkinson (2005) among many others). Moreover, both adjusting ground motion models for specific sites and assessing site-specific seismic hazard require consideration of near-surface attenuation. For example, the ground motion scaling from rock-sites, assumed as reference, to sites characterized by other lithologies is made by taking into account both site amplification, which is dominant at frequencies comparable with the fundamental soil frequency, and site attenuation that dominates higher frequencies (Laurendeau et al. 2013; Al Atik et al. 2014; Ktenidou & Abrahamson 2016). Finally, in seismological studies concerning seismic sources, or attenuation properties in specific regions, removal of the attenuation term due to wave

propagation through the shallowest material beneath the recording site is a key step in investigating source and path properties (see Bindi et al. (2004); Castro et al. (2008); Oth et al. (2011) or Castro et al. (2013) among many others).

Attenuation of seismic waves can be quantified by different parameters. The quality factor, Q , has been introduced in seismology with the aim of quantifying the fractional energy loss per cycle of oscillation as: $Q = 2\pi E/\Delta E$ (Knopoff 1964). The material damping, ξ , related to the quality factor by: $\xi = 1/2Q$, is generally employed in geotechnical engineering. ξ is defined in terms of the ratio between the energy dissipated per cycle and maximum stored energy per cycle, during a stress-strain loop of a Kelvin-Voigt solid (Kramer 1996). Regarding high frequency attenuation, in both seismology and earthquake engineering the spectral decay parameter kappa (k), an empirical parameter introduced by Anderson & Hough (1984), is customarily used to quantify the high frequency spectral decay of the Fourier Amplitude Spectrum (FAS) of ground acceleration. They observed that in linear-logarithmic space, the acceleration FAS can be assumed to decay linearly for frequencies above a certain value, f_e , and modeled the spectral amplitude as: $A(f) \propto A_0 e^{-k\pi f}$ for $f > f_e$. Anderson & Hough (1984) also observed that for each station, the measured values of k (hereinafter referred to as “ k -record values”) scale with distance. They named k_0 the zero-distance intercept of the trend of k versus epicentral distance, R_e . Assuming a simplified stratigraphy consisting of layers with relatively strong attenuation properties overlying deeper less attenuating materials, k_0 corresponds to the attenuation that S-waves encounter when traveling almost vertically through the geological structure beneath the site. On the other hand, given a set of recording stations, the distance-dependent contribution common to all paths from the source to the site would be associated with the deeper, predominantly horizontal propagation of S-waves through the crust (Hough et al. 1988; Anderson 1991). The regional attenuation model is generally modeled by: $k(R_e) = k_0 + m \cdot R_e$, in which the linear increase of k with R_e , parameterized by the slope m , is assumed as a good approximation of the observed trend (Anderson 1991; Fernández et al. 2010; Douglas et al. 2010; Gentili & Franceschina 2011; Ktenidou et al. 2013). Regarding k_0 , the most widely accepted point of view is that site conditions have the key role in determining this parameter. Therefore, it is usually referred to as the site component of k or “site-specific kappa” (Ktenidou et al. 2014, 2015; Perron et al. 2017).

Regarding ground motion modeling, both k and Q can be used as parameters in the frequency-dependent term that accounts for the attenuation of Fourier spectral ordinates along the whole path from source to site. The site response is then modeled by a frequency-dependent transfer function that represents the amplification/de-amplification effects of seismic waves as

they travel vertically through the subsurface geological structure beneath the site. Empirical estimates of site transfer functions generally show amplification peaks of various amplitude and shape at frequencies comparable with the fundamental soil frequency. At higher frequencies, the dominant effect of the surface stratigraphy consists of a diminution of the spectral amplitude with respect to frequency (spectral decay). For seismic design purposes, it must be considered that strong ground shaking is mainly governed by shear(S)-waves. S-wave velocity, V_S , and S-wave quality factor, Q_S , are then usually taken into account in numerical simulations and, in the last decades, different low-cost non-invasive experimental techniques have been developed in order to obtain V_S profiles in shallow deposits up to tens of meters deep. On the contrary, Q_S measures at shallow depths are much less common. Indeed, attenuation of surface deposits is often evaluated through measures of shear strain-dependent damping, ξ , obtained from laboratory tests on small-scale soil samples. These tests can only capture intrinsic material damping, which implies that other causes of attenuation (e.g., scattering effects) cannot be quantified in such conditions. As a consequence, site response predictions performed at low level of strain, based on field measures of V_S and damping profiles provided by geotechnical laboratory testing, may lead to an over-prediction of the estimated ground motion. A comprehensive review on this topic can be found in Parolai et al. (2022). However, S-wave attenuation of surface deposits can also be evaluated through estimates of k_0 , therefore using measures of the ground motion recorded in the field. Only recently, researchers obtained estimates of k_0 using data collected with borehole sensors and quantified the differences between field attenuation estimates and laboratory-based damping models (Ktenidou et al. 2013, 2015; Lai et al. 2016; Pilz & Fäh 2017; Cabas & Rodriguez-Marek 2017; Cabas et al. 2017; Xu et al. 2020).

In this work, we analyze data from a microseismic network composed of three surface and four 100-m deep borehole stations that sampled an almost uniform lithological condition in the central Po Plain (northern Italy) with the aim of estimating high-frequency S-wave attenuation in the field. Using earthquake data collected during a two-year recording period of the network, we estimate an average value of Q_S of the uppermost 100 m of surface deposits. For this purpose, we estimate $\Delta k_{0,100}$, the difference between the values of k estimated at the surface and at the boreholes depth, respectively, and evaluate an average value of V_S of the above-mentioned stratigraphy. This second goal is pursued by exploiting the seismic wave interference between the incident and surface-reflected waves, which modifies the shape of amplitude Fourier spectra observed at depth. In order to constraint the influence of the high variability generally observed in the distribution of the k -record values, we implement

different inversion strategies to estimate $\Delta k_{0_{100}}$, which we expect to give similar results but with increasing accuracy. Finally, we also estimate the regional attenuation model of k in terms of k increment with epicentral distance and, for either surface and borehole stations, we compute the site-specific kappa, k_0 .

2 STUDY AREA

The Po Plain (northern Italy), one of the largest alluvial basins in the world (45,000 km²), is bounded by the Alps and Apennines to the north and south, respectively, and is everywhere characterized by the presence of deep sediments with soft upper layers. Indeed, the thickness of the Plio-Pleistocene sedimentary succession, that directly overlies the deep Miocene sedimentary rock and extends over the whole area, can reach 7000-8000 m at depocenters (Bigi et al. 1992; Martelli et al. 2017). The region is affected by a general compressive regime, with south-verging thrust systems in the central-eastern Southern Alps and buried north-verging active thrusts in the Northern Apennines (Carminati & Doglioni 2012). Historical and current seismicity is observed both at the Pedepennine Thrust Front, which borders the entire Po Plain to the south, and in the central-eastern Southern Alps, with maximum magnitudes decreasing from east to west (see Data Availability and Resources). The study area is located in the central part of the Po Plain (Fig. 1), between the Pedepenninic Thrust Front and the Emilia arc, where the continental to marine sedimentary layers, forming the Plio-Quaternary succession, reach a maximum depth of 2000-3000 m (Fantoni & Franciosi 2010). The surface geology of the area is characterized by a continental succession belonging to the Pleistocene-Holocene corresponding to two main depositional cycles, known as upper synthem and lower synthem (Martelli et al. 2017). Seismic reflection and borehole data acquired for hydrocarbon exploration in the 1970s and 1980s, subsequently integrated with sedimentological observations enable highlighting two main geological unconformities within the Plio-Quaternary sediments, known as the R-surface and the Y-surface. The former defines the base of the continental succession (0.87 Ma) and the latter bounds the base of the upper synthem (Martelli et al. 2017). R-surface and Y-surface are mapped throughout the entire Po Plain, with the former that ranges from about 100 m above sea level in the western sector to 600 m below sea level in the central plain, and the latter that ranges from 100 m above sea level in the western sector to 300 m below sea level in the central plain (Scardia et al. 2012). Indeed, passive seismic prospecting, based on environmental vibration measurements carried out throughout the entire Po Plain, highlights V_S profiles that can be well correlated with the aforementioned geological unconformities (Paolucci et al. 2015; Mascandola et al. 2019).

In the framework of a pilot project for CO_2 geo-sequestration (Augliera et al. 2012), a microseismic network, consisting of three surface and four 100-m deep borehole sensors, operated in this area in the period February 2010 - April 2012 (see Fig. 1 and Table 1). The network covered a $6 \times 2 \text{ km}^2$ area sampling a presumably uniform lithological condition, with minimum inter-station distances ranging from 0.6 to 2.6 km. According to Scardia et al. (2012), in this area the Y-surface gradually deepens moving from SSW to NNE with depths ranging from about 50 to 150 m. Moving in the same direction, the surface topography shows a gradual decrease, with elevation values ranging approximately from 60 to 40 m. Considering that station elevations were in the range 44-52 m (see Table 1), we can assume that all 100-m deep borehole sensors were installed within a common sedimentary layer, extending from the Y-surface to the topographic surface. Moreover, the almost uniform lithology of the area, also allows to suppose that the stations were characterized by a similar S-wave velocity profile. These issues will be addressed in detail in the next sections. All stations were composed of 24-bit digital recorders (Lennartz M24/NET) equipped with a GPS time receiver. Lennartz LE-3D/BH and Lennartz LE-3Dlite MkII sensors were used for borehole and surface installations, respectively (see Data Availability and Resources). The borehole and surface sensors had similar characteristics, with 136 dB dynamic range, 1-80 Hz band-pass frequency and 400 V/m/s sensitivity (Table 1). Data acquisition was operated in continuous mode at 100 Hz sampling frequency. Seismic noise recorded over a two-year period shows that, in the frequency band 1-25 Hz, surface stations were characterized by an average level of velocity power spectral density of about -145 dB with respect to $1 \text{ (m/s)}^2/\text{Hz}$, with annual and monthly variability around 10 and 20 dB, respectively. Borehole installations reduced the average recorded noise to approximately -155 dB and limited the annual and monthly variability to approximately 5 and 10 dB, respectively (Franceschina et al. 2015).

3 DATA SELECTION

Starting from continuous data collected by the microseismic network described above, we selected two data-sets (selections 1 and 2) in order to compute the k -record values. First, in order to comply to the already outlined conceptual framework of horizontal propagation in the crust and vertical propagation beneath the site, we choose the events with hypocentral depth less than 25 km and epicentral distance from the center of our network less than 350 km. As seen in Fig. 1, the stations were installed in an urbanized area with highways and railways nearby, which implies the significant level of seismic noise reported in Section 2. Therefore, an empirical threshold of local magnitude given by: $M_{L_t} > 2.1 \log R - 2$, where R repre-

sents the hypocentral distance, is applied. Event locations and magnitudes are taken from the Italian National Earthquake Observatory website (see Data Availability and Resources). From the resulting recordings, only those with the signal-to-noise ratio greater than 3 (see eq. (16)) are retained to end up with our selection 1, consisting of 941 recordings from 244 events. Corresponding earthquakes have epicentral distances ranging from 6 to 347 km and local magnitudes in the range 1.3-4.5. Afterwards, some more events with hypocentral depth greater than 25 km are considered for the analyses, described below, where only the vertical propagation beneath the site matters. This further selection consists of 124 recordings from 27 events. We define as selection 2 the data selection composed by the data of this last selection and those of selection 1. Earthquakes corresponding to selection 2 extend the range of local magnitudes up to $M_L=4.9$. Fig. 2, which shows the distribution of event magnitudes and hypocentral depths with respect to epicentral distances, depicts a data-set with 50% of magnitudes in the range 2.4 to 3.2 and 50% epicentral distances clustered between 40 and 70 km. The influence of these features on k estimation and on the estimation of the k trend with distance, will be addressed later on. Conversely, the moderate-to-strong correlation between magnitude and epicentral distance pointed out in Fig. 2 (correlation coefficient is about 0.6) prevents any investigation on the k dependence on magnitude. However, both surface and borehole k values would be equally affected by a possible dependence on magnitude, and this would produce an unbiased estimate of $\Delta k_{0_{100}}$, which is the main focus of this work.

Horizontal-to-vertical spectral ratio on noise (HVSR), shown in Fig. 3, provide an appraisal of site effects for the surface stations. HVSRs are computed on some long samples of noise, using time windows of 328 and 41 s for the representations in the low (0-2 Hz) and high (0-40 Hz) frequency ranges, respectively. Smoothing half-windows are 0.15 and 1.80 Hz, respectively. In particular, in the low frequency range the computed HVSRs display a spectral shape which is typical of sites located in a large part of the Po Plain (Fig. 3 - Inner panel). Indeed, according to Mascandola et al. (2019), a number of sites located all over the Po Plain show a double-peak in the low frequency HVSRs, with the highest-frequency peak which seems to be correlated to a significant S-wave velocity discontinuity, roughly corresponding, in our area, to the Y-surface above described (see Figs. 4 and 6 in Mascandola et al. (2019)). By applying the relationship between the frequency of the peak and the depth of the discontinuity developed by Mascandola et al. (2019), and considering an upper limit of 0.75 Hz for the highest frequency peaks of our surface stations, we obtain a lower bound of about 100 m for the 95% prediction interval of the depth of the discontinuity. Therefore, the borehole stations must have been positioned in the sediments indeed, with only some uncertainty concerning

C127, which is located slightly away from the area encompassed by the surface stations. As regards the high frequency range, the HVSR of station C001 shows a significant amplification between 14 and 18 Hz (see Fig. 3), which would likely result in a biased assessment of the corresponding kappa value. We nevertheless employ the data recorded by this station and use the corresponding results for comparison purposes. For the same reason, we also present the results obtained with borehole station C047, whose NS component was damaged and thus unusable starting from a few weeks after the installation date. For this station we use the EW component only.

4 METHOD OF ANALYSIS

An average value of Q_S that characterizes a sedimentary stratigraphy of overall thickness H , can be defined as:

$$Q_{S,H} = \frac{H}{\int_0^H \frac{dh}{Q_S(h)}} \quad (1)$$

where $Q_S(h)$ represents the average Q_S profile of the area. In this work, we evaluate eq. (1) with $H = 100$ m, by considering: (1) high frequency attenuation of seismic waves due to propagation through the uppermost 100 m sedimentary layers and (2) seismic wave interference between the incident and surface-reflected waves. The former is parameterized through $\Delta k_{0,100} = k^{surf} - k^{bore}$, the difference between the values of k estimated at the surface and at the boreholes depth, respectively. The latter is exploited in order to evaluate an average value of S-wave velocity of the uppermost 100 m in terms of time-averaged S-wave velocity, $V_{S,100}$.

To obtain $\Delta k_{0,100}$, it is necessary to introduce a spectral model for the acceleration FAS, from which we can estimate both k^{surf} and k^{bore} through the measurement of the k -records. Moreover, we introduce a regional model for the k increase with epicentral distance. This latter model allows deriving estimates of site-specific kappa at the surface and at the depth of the boreholes, k_0^{surf} and k_0^{bore} respectively, which, for any assigned station J , we named k_0^J . The k_0^J values obtained with surface and borehole stations are used to estimate $\Delta k_{0,100}$ which represents the average high frequency attenuation of the area in the uppermost 100 m. Note that both k^{surf} and k^{bore} depend on the contribution to high frequency attenuation of the whole path, from source to site. Conversely, $\Delta k_{0,100}$ being an average value referred to the installation area of the network, we expect it is unaffected by the source-to-site path for sufficiently large (> 10 km) epicentral distances.

As regards $V_{S,100}$, one of the first experimental evidences of seismic waves interference was reported by Tucker et al. (1984) who explained the observed “holes” in the Fourier spectrum measured at depth at frequencies f_N ($N = 0, 1, \dots$), in terms of destructive interference of incident and surface-reflected waves. Recently, this phenomenon has also been exploited to validate the shallow V_S model at the site of Mirandola (Italy) (Laurenzano et al. 2017). Indeed, for each borehole station J , accurate measures of the difference between two adjacent interference frequencies, $\Delta f_{N,N+1}^J = f_{N+1}^J - f_N^J$, make it possible to deduce the time-averaged value of V_S referred to that station, $V_{S,100}^J$.

Below we present: (1) the spectral model and the procedure used for the measurement of the k -records (Sections 4.1 and 4.2); (2) the regional model for the k increase with distance and the procedures employed to estimate k_0^J and $\Delta k_{0,100}$ (Section 4.3); (3) the method used for estimating $V_{S,100}^J$ from the measure of interference frequencies (Section 4.4) and (4) the method for estimating $V_{S,100}$ and $Q_{S,100}$. The latter is computed from eq. (1) using the above estimates of $\Delta k_{0,100}$ and $V_{S,100}$ (Section 4.5).

4.1 Spectral model

The acceleration spectral amplitude at frequency f and hypocentral distance R , is modeled as:

$$U_A(f, R) = S(f) \cdot A(f, R) \cdot Z(f) \quad (2)$$

where $S(f)$, $A(f, R)$ and $Z(f)$ represent the source, attenuation and site response terms, respectively. The attenuation term can be written as:

$$A(f, R) = G(R) \cdot e^{-\frac{\pi f R}{V_S Q_S(f)}} \quad (3)$$

where Q_S and V_S are the average S-wave quality factor and S-wave velocity along the ray path, respectively, and $G(R)$ represents the geometrical spreading. Investigation on the high frequency attenuation can be addressed by introducing the spectral decay parameter $k(R)$ and, following Gentili & Franceschina (2011), relating it to the quality factor through:

$$\frac{1}{Q_S(f)} = \frac{1}{Q_{S_i}} + \frac{1}{Q_{S_d}(f)} \quad (4)$$

and:

$$k(R) = R/(Q_{S_i} \cdot V_S) \quad (5)$$

where Q_{S_i} and $Q_{S_d}(f)$ represent the frequency-independent and the frequency-dependent parts of the S-wave quality factor, respectively, averaged over the whole path. A similar approach was adopted by Hough et al. (1988), who stressed that eq. (4) does not represent the separation between physical mechanisms responsible for attenuation. Indeed, scattering and intrinsic attenuation can contribute to both terms. In eq. (4), the second term represents the contribution to attenuation due to the low frequency part of the spectrum, usually parameterized as:

$$Q_{S_d}(f) = Q_0 f^n \quad (6)$$

According to eqs. (4) and (6), at high frequencies ($f > 10 - 15$ Hz) the quality factor tends to become independent on frequency, and at low frequencies, over any limited frequency band, the frequency dependence can be parameterized by an appropriate choice of Q_0 and n . These properties have been confirmed by many experimental studies performed in different regions (see Bindi et al. (2004); Castro et al. (2008, 2013) or Li et al. (2020) among many others).

4.2 Spectral decay parameter estimation

We estimate k adopting an “acceleration spectrum” method (Ktenidou et al. 2014), where k -record values are directly measured in linear-logarithmic space on the high-frequency part of the Fourier acceleration spectrum of the S-waves. Generally, both horizontal components are used to estimate this parameter, and different strategies are adopted to consider k_{NS} and k_{WE} , the k values obtained from NS and WE components, respectively. In this work, we do not estimate k_{NS} and k_{WE} but, following Tumarkin & Archuleta (1997), make use of the complex representation of horizontal ground motion in order to compute the maximized spectrum (MS) introduced by Shoja-Taheri & Bolt (1977). According to Shoja-Taheri & Bolt (1977), the MS is a more satisfactory spectral representation of the overall ground motion with respect to Fourier amplitude spectra computed with the individual horizontal components or with vectorial compositions of the two. Indeed, according to Steidl et al. (1996), the MS provides the total amplitude of horizontal motion at a given frequency, preserving the phase between components (see also Perron et al. 2017). For each selected earthquake I , recorded at station J , we compute the corresponding k -record, $k^{I,J}$, considering the slope of the high frequency part of the acceleration MS. The step-by-step procedure of the $k^{I,J}$ calculation used

in this work can be summarized as follows. The horizontal components of velocity data are used to compute the acceleration MS of S-waves by selecting time windows starting at the direct S-wave onset and including the significant part of the ground motion. We manually pick P- and S-wave onsets and also select an equal-length time window for noise analysis before the first P-wave arrival. Only direct S-waves should be used for the k estimation, as scattered waves and in some cases also surface waves perturb the selected windows. A 0.5 s duration window of tapered data is added to both sides of the selected window and the resulting time sequence is padded with zeros before applying the FFT algorithm. Depending on magnitude and distance of the event, variable-length windows are adopted. The distribution of the length of time windows employed in this work is reported in Table 2. The obtained acceleration MS is then used to estimate $k^{I,J}$ through a linear regression of the spectral amplitudes between frequencies f_A and f_B in linear-logarithmic space. The spectral band adopted for the analysis is determined by selecting the part of the spectrum where a linear decay is clearly evident. For each record, f_A is chosen by plotting the $k^{I,J}$ values obtained with different values of this parameter and selecting $k^{I,J}$ in an observed range of stability of the function $k^{I,J}(f_A)$ through a visual inspection of each plot. Fig. 4 shows an example of k -record estimation. Other examples can be found in the supplementary data.

In order to estimate k -record, we take care in picking f_A by considering a hypothetical value for the corner frequency of the corresponding earthquake, f_c , in order to avoid the trade-off between attenuation and source effects. Dealing with small magnitude events ($1.3 \leq M_L \leq 4.9$), we hypothesize a scaling between seismic moment, M_0 , and corner frequency, f_c , given by: $M_0 \propto f_c^{-(3+\epsilon)}$, where the ϵ value is chosen based on recent results on scaling laws of Italian regions. Many papers on this topic show evidence of $\epsilon > 0$ and of low stress drop values for moderate magnitude earthquakes (Franceschina et al. 2006; Malagnini et al. 2008; Calderoni et al. 2013; Castro et al. 2013; Franceschina et al. 2013; Pacor et al. 2016; Malagnini & Munafò 2018). In the present work, in which earthquakes in northern Italy are analyzed, we approximately assess, for instance, f_c values of 5.2 and 8.6 Hz for $M_L = 2.0$ and $M_L = 1.0$, respectively, assuming $\epsilon = 1.6$ and a 1:1 scaling between M_L and the logarithm of the moment. Table 2 shows that about 25% of the chosen f_A is less than the corresponding estimated value of f_c . However, we also include these cases in the outcomes of this work as source effects should not significantly affect the estimates of $\Delta k_{0.100}$, as will be illustrated in Section 4.3. As for f_B , by visually inspecting the MS signal superimposed on the respective MS noise, we choose it to be lower than the frequency at which the noise level begins to contaminate the signal (see Fig.4). In this regard, it is worth recalling that, on average, borehole stations

have noise levels about 10 dB lower than surface stations (see Section 2). In picking both f_A and f_B , we also try to avoid biasing k measurement due to distortions of the expected linear trend, produced by resonant peaks of the site transfer function (Parolai & Bindi 2004). This strategy can easily be applied only for surface stations that do not exhibit local amplification effects, like C073 or C134. For station C001, probably affected by a limited amplification effect in the frequency band [14-18] Hz (see Fig. 3), it is more difficult to obtain unbiased estimates of the k parameter. Nevertheless, we include in the outcomes of the work also the estimates of k -record obtained with C001, aiming to compare the overall results obtained with or without this station. Finally, when picking f_A and f_B we discard the data with the resulting frequency bandwidth lower than the empirically established limit of 5 Hz. Table 2 reports the employed distributions of f_B and of $(f_B - f_A)$, together with the distribution of the obtained signal-to-noise ratio s/n , computed by considering the MS of signal and noise in the frequency band: $[f_A, f_B]$. It is apparent from the table that only 20% of the records is characterized by $f_B - f_A \leq 8$ Hz and only 20% has: $3.0 \leq s/n \leq 4.5$.

4.3 Site-specific kappa and seismic wave attenuation in the upper 100 m

Considering the dependence of Q_{S_i} and V_S on the ray path, Γ , eq. (5) can be generalized as:

$$k(\Gamma) = \int_{s \in \Gamma} \frac{ds}{Q_{S_i}(s) \cdot V_S(s)} \quad (7)$$

Since k values measured at a given station show an increase with epicentral distance, eq. (7) is parameterized in terms of site-specific kappa, k_0 , and distance-dependent component of kappa, $\tilde{k}(R_e)$, according to:

$$k(R_e) = k_0 + \tilde{k}(R_e) \quad (8)$$

Recently, k_0 has been written as the sum of two contributions: Δk , the upper local attenuation caused by the shallow sedimentary layers beneath the receiver and $k_{0_{ref}}$, related to the regional (reference) hard-rock attenuation beneath the receiver (Edwards et al. 2013; Ktenidou et al. 2015; Mayor et al. 2018). $\tilde{k}(R_e)$, corresponding to the incremental attenuation due to predominantly horizontal S-wave propagation through the crust, is generally written as: $\tilde{k}(R_e) = m \cdot R_e$. In this case, according to eq. (7) the slope m of the linear increase of k with epicentral distance can be related to Q_{S_i} and V_S average values along the deepest part of the ray path. In this work, we indicate Δk as Δk_0 and, assuming that borehole stations are installed in the shallowest part of the sedimentary layers, we write eq.(8) as:

$$k(R_e) = \Delta k_{0_{100}} + \Delta k_{0_X} + k_{0_{ref}} + m \cdot R_e \quad (9)$$

where $\Delta k_{0_{100}}$ and Δk_{0_X} are the contributions to local attenuation caused by sedimentary layers located in the shallowest 100 m stratigraphy and by sedimentary layers located from the borehole depth to bedrock, respectively. Seismic stations installed over a common bedrock but with different configurations of underlying sedimentary layers, will display different values of k_0 due to the different contributions of the quantity: $(\Delta k_{0_{100}} + \Delta k_{0_X})$. Besides being installed over a common bedrock, the stations used in this work can also be considered as having similar values of Δk_{0_X} . So, we expect them to show different values of k_0 due to different values of $\Delta k_{0_{100}}$. This condition is ensured by the small inter-station distances and by the stratigraphic homogeneity of the installation area of the network. Therefore, in order to estimate $\Delta k_{0_{100}}$, we choose a reference borehole station and its corresponding site-specific kappa, k_0^{REF} , defined as:

$$k_0^{REF} = \Delta k_{0_X}^{REF} + k_{0_{ref}} \quad (10)$$

Consequently, named as $\Delta k_{0_{100}}^J$ the value of $\Delta k_{0_{100}}$ estimated at station J , the corresponding site-specific kappa is given by:

$$k_0^J = \Delta k_{0_{100}}^J + k_0^{REF} \quad (11)$$

with $\Delta k_{0_{100}}^J \cong 0$ for borehole stations and $\Delta k_{0_{100}}^J \cong \Delta k_{0_{100}}$ for surface stations. Note that $\Delta k_{0_{100}}^{REF} = 0$ by definition.

In order to reduce the influence of the high variability of k -records and bearing in mind that our final goal is the evaluation of $\Delta k_{0_{100}}$, we have implemented four different methods, which progressively include some elements of improvement, to calculate $\Delta k_{0_{100}}^J$, k_0^J and m (see supplementary data for the details). In method (A) we use data selection 1 and, adopting a standard procedure, for each station J we assume a specific linear dependence of k on epicentral distance, parameterized by the slope m^J . In method (B) we exploit the network configuration which implies much greater epicentral distances than inter-station distances and thus a distance dependence of k which is expected to be the same for all stations. Therefore, after having verified this hypothesis by method (A), with this second method we perform a linear regression of the data of selection 1 by assuming the same slope (m) for all stations. Method (C) is introduced with the aim of minimizing the bias due to source effect (f_c) and crustal attenuation on $\Delta k_{0_{100}}$. The method relies on direct estimation of $\Delta k_{0_{100}}^J$, performed

with the data of selection 2 recorded simultaneously from any station and from the reference and this implies a general reduction in available events. In order to avoid this drawback, we finally apply method (D), where a generalized inversion technique is applied to the k -record data-set in order to separate each $k^{I,J}$ into the contributions of an average event k , \bar{k}^I , and a corresponding residual, $\Delta k_{0_{100}}^J$. We assume that \bar{k}^I is characterized by a linear dependence on epicentral distance measured from the center of the network, R_e^C . Note that the above four methodologies avoid grouping the stations in accordance with their category: surface or borehole station. We apply precisely this strategy to be able to use kappa estimation as validation of membership in a given site category. Moreover, besides $\Delta k_{0_{100}}^J$, k_0^J and m (or m^J), the above methods allow us to compute the root-mean-squared error, e_k , on the function $k^J(R_e^J)$, which represents the linear increase of k with epicentral distance.

Finally, we estimate the average high frequency attenuation of the area in the uppermost 100 m in terms of $\Delta k_{0_{100}}$, computed as the difference between the weighted means of the k_0^J values of surface and borehole stations, respectively. Furthermore, being interested in the characterization of the areal variability of this parameter, we evaluate the uncertainty on $\Delta k_{0_{100}}$ in terms of standard deviation.

4.4 Seismic wave interference and S-wave velocity in the upper 100 m

In the case of homogeneous medium with vertically incident S-waves, the frequency difference between two adjacent interference holes, Δf , observed in the spectrum at depth H , can be related to S-wave velocity, V_S , by: $\Delta f = V_S / (2 \cdot H)$ (Tucker et al. 1984; Laurenzano et al. 2017). In the more realistic case of an inhomogeneous medium, the interferometric function cannot be written in simple form. However, for sites where the rigidity is mainly controlled by lithostatic pressure, the velocity profile is not expected to be characterized by strong discontinuities. In such cases, the above relation can be applied to the time-averaged S-wave velocity, $V_{S,H}$, and thus written as:

$$\Delta f = \frac{V_{S,H}}{2 \cdot H} \quad (12)$$

Section 6.1 provides additional details on this issue. In order to apply eq. (12), we compute the MS of velocity data recorded by borehole stations. We use velocity spectrum to better highlight interference holes, which are mainly readable in the low-frequency range. The S-wave MS is calculated as in Section 4.2. As regards the windows duration, it is worth noting that, by considering a lower limit of about 200 m/s for the average V_S of the upper sedimentary

stratigraphy, we obtain an upper limit of 1 s for the time-delay due to propagation of the direct and surface-reflected waves. This implies time-windows longer than 1 s to observe interference holes. However, in this work we avoid selecting overly long windows, that probably include waves different from the direct or the surface-reflected waves producing interference. Assuming a vertical propagation, for each selected earthquake I , recorded at the borehole station J , we measure the frequencies $f_N^{I,J}$ where seismic wave interference produces spectral holes on the corresponding MS. Fig. 5 shows an example of interference frequencies estimation. Other examples are shown in the supplementary data. For each record we superimposed the original MS, the smoothed MS and the MS of noise, computed by considering an equal-length time window selected before the first P-wave arrival. We consider up to 5 frequencies $f_N^{I,J}$ with: $N = 0, \dots, 4$. We then compute the frequency difference between two adjacent holes observed at each station, Δf^J (see supplementary data for the details) and use these values in eq. (12) in order to estimate $V_{S,100}^J$, the average S-wave velocity of the uppermost 100 m sedimentary column overlying station J . We set: $H = 100$ m and, to compute the standard errors $\sigma_{V_{S,100}^J}$, we assume: $\delta H = 1.5$ m.

4.5 S-wave velocity and quality factor of the area

The S-wave quality factor of the area is estimated in terms of $Q_{S,100}$, after having computed $V_{S,100}$ as weighted mean of the $V_{S,100}^J$ values obtained with borehole stations. As already done for $\Delta k_{0,100}$, also uncertainty of $V_{S,100}$ has been characterized by the corresponding standard deviation. The estimates of $\Delta k_{0,100}$ and $V_{S,100}$ are then employed to compute $Q_{S,100}$ through eq. (7). For this purpose, we consider S-waves that propagate vertically through wave velocity and quality factor profiles: $V_S(h)$, and $Q_S(h)$, respectively. For the area investigated we assume $V_S(h)/Q_S(h)$ independent of depth, h , and a depth dependence of V_S given by: $V_S(h) = V_{S_0} (1 + h/h_{ref})^x$, where V_{S_0} represents the zero-depth S-wave velocity, x gives the depth dependence and $h_{ref} = 1$ m. This kind of depth dependence, which is generally assumed for sites where the rigidity is mainly controlled by lithostatic pressure, is suitable for the area under investigation (Ibs-von Seht & Wohlenberg 1999; Paolucci et al. 2015; Mascandola et al. 2019). With these assumptions eq. (7) can be written as:

$$\Delta k_{0_H} = \frac{h_{ref}}{V_{S_0} Q_{S_0}} \cdot \frac{[1 + (H/h_{ref})]^{1-2x} - 1}{1 - 2x} \quad (13)$$

where Q_{S_0} represents the zero-depth quality factor and H is the length of the vertical profile.

With the same assumptions, eq. (1) and the time-averaged S-wave velocity become:

$$Q_{S,H} = \frac{Q_{S_0} (H/h_{ref}) (1-x)}{[1 + (H/h_{ref})]^{1-x} - 1} \quad (14)$$

and:

$$V_{S,H} = \frac{V_{S_0} (H/h_{ref}) (1-x)}{[1 + (H/h_{ref})]^{1-x} - 1} \quad (15)$$

respectively. We apply the equations above to the uppermost 100 m of the sedimentary stratigraphy underlying the installation area of the network by setting: $H = 100$ m. Considering eq. (15) with a specific depth dependence (x) inferred from a mean V_S profile representative of the Po Plain (Mascandola et al. 2019), we employ the measure of $V_{S,100}$ to calculate V_{S_0} . Next, we use the measure of $\Delta k_{0,100}$ in eq. (13) to calculate Q_{S_0} and finally eq. (14) to obtain the estimate of $Q_{S,100}$. In order to characterize the variability of these parameters in the studied area, we evaluate all uncertainties in terms of standard deviations. Note that $Q_{S,100}$ is independent of frequency and, according to Ktenidou et al. (2015) and Cabas et al. (2017), it accounts for both intrinsic attenuation and attenuation due to scattering.

5 RESULTS

The spectral analysis of 1065 velocity data, collected in the period February 2010 - April 2012 by the microseismic network described in Section 2, allows estimating the values of k -record from the slope of the high frequency part of the corresponding MS (see Section 4.2). We obtain k -record values in the range 44–149 ms, characterized by uncertainties ranging from 1 to 21 ms, homogeneously distributed with respect to magnitude and distance. It is worth recalling that the MS is a more satisfactory spectral representation of the overall ground motion with respect to Fourier amplitude spectra computed with the individual horizontal components. Many tests performed with different subsets of the final data-set, allowed us to establish that this method generally produces more stable estimates of k with respect to other methods, such as computing the k value by averaging the individual horizontal components, or by using the horizontal component corresponding to the polarization angle which provides the maximum ground motion energy. k -record values and uncertainties are comparable with the results generally found in the literature (see Anderson (1991); Fernández et al. (2010); Douglas et al. (2010); Gentili & Franceschina (2011); Ktenidou et al. (2013, 2014, 2015) or Perron et al. (2017) among many others) and we consider the obtained results as sufficiently reliable to calculate $\Delta k_{0,100}$. In the following, we present the results concerning the estimation of k_0^J , m (or m^J) and $\Delta k_{0,100}^J$. Note that, although the estimate of the slope of the linear trend of

k with distance does not represent one of the main tasks of the work, an incorrect estimation of m can affect the measure of k_0^J . Moreover, since our network did not have co-located stations at surface and depth, each $\Delta k_{0,100}^J$ depends on the whole network configuration. We also present the outcomes regarding the estimation of the interference frequencies employed to infer $V_{S,100}^J$, the time-averaged value of S-wave velocity of the uppermost 100 m, measured with each of the borehole stations. 579 values of interference frequencies are estimated from the data recorded by borehole stations. Finally, we present the results concerning the main task of the work: the estimation of $V_{S,100}$ and $Q_{S,100}$, the S-wave velocity and quality factor of the area referred to the uppermost 100 m of sedimentary layer.

5.1 Estimates of site-specific kappa and $\Delta k_{0,100}$

Fig. 6 shows the results obtained by applying methods (A) and (B) to infer the linear dependence of k on epicentral distance. Table 3 lists the corresponding values of k_0^J , m (or m^J) and $\Delta k_{0,100}^J$ with the related standard errors. The figure shows that, as found in recent works, the estimates of k -record are characterized by elevated dispersion (see Mayor et al. (2018); Castro et al. (2019); Li et al. (2020) or Xu et al. (2020) among many others). However, the large number of data used in the regressions enables limiting the uncertainties on the site-specific kappa. We obtain percentage errors in the ranges [3, 7] % and [2, 4] % with methods (A) and (B), respectively. Comparison of the regressions obtained with these two methods shows that only for stations C047 and C012, at distances greater than about 200 km, is the best estimate of the k parameter obtained with one method outside the 95% confidence limits obtained with the other. The dataset used is in fact characterized by an elevated density of data between 40 and 50 km and it shows a particular paucity of data beyond 250 km. The application of methods (A) and (B) provides values of $\Delta k_{0,100}^J$ in accordance with the corresponding station-depth for all stations of the network, except for C001 and C047 (see Table 3). Note that, by applying method (B) without considering these stations, we do not obtain significant changes in the results. Otherwise, the similar trend of k with epicentral distance obtained with these methods confirms the validity of the constraint adopted in methods (B), (C) and (D), that, because of the small distance between stations relative to the epicentral distance, all stations should show a linear trend described by the same slope.

Fig. 7 shows the results obtained by applying methods (C) and (D). The corresponding values of k_0^J , m and $\Delta k_{0,100}^J$ are listed in Table 3. Both methods provide a m value of 0.08 ms/km, strictly compatible with the value of 0.07 ms/km obtained with method (B). As regards methods (C) and (D), we employ the k -records obtained from selection 2, thus

exploiting the larger number of data of this dataset (1010 values of k -record corresponding to 216 events). Fig. 7 still highlights the high dispersion that characterizes the k -record estimates, but confirms the stability of the slope of the linear trend representing the increase of k with distance. As already found with methods (A) and (B), also methods (C) and (D) show accordance between site-specific kappa and station-depth for all stations of the network, except for C001 and C047.

The estimates of k_0^J , m (or m^J) and $\Delta k_{0,100}^J$ obtained with all methods are compared in Fig. 8. As already noted, the estimates of m are particularly stable, especially when methods (B), (C) or (D) are applied (see Fig. 8: upper panel). Moreover, methods (A) and (B) provide results depending on the different distribution of data of each station with respect to epicentral distance. This property is particularly apparent when method (A) is applied. Stations C012 and C047 for example, show m^J values which are significantly different with respect to those obtained with the other stations, probably due to the paucity of k -record estimates at large distances (see Fig. 8: upper panel). The same stations also show a lesser match between k_0^J values estimated by these two methods and those obtained by methods (C) and (D) (see Fig. 8: central panel). Indeed, methods (C) and (D) are not affected by this drawback and can exploit the larger number of data of selection 2. Moreover, method (D) uses more data than method (C) because it is not constrained by the selection of data in temporal coincidence with the reference station (see Table 3: column 9). The estimates of k_0^J and $\Delta k_{0,100}^J$ show a trend which is common to all methods and, as regards $\Delta k_{0,100}^J$, methods (C) and (D) appear to be highly compatible while methods (A) and (B) show less accordance with the common result of (C) and (D). As previously noted, all methods show, for C047, a $\Delta k_{0,100}^J$ value which could be characteristic of a surface station, and for C001 a value which could be typical of a borehole station. As mentioned above, the estimates of k -record obtained with data from these stations may have been influenced by site effects or instrument malfunctions. Table 3, however, also shows that the exclusion of stations C001 and C047 does not significantly affect the estimates of m , k_0^J and $\Delta k_{0,100}^J$ obtained by methods (B), (C) and (D).

5.2 Estimates of $V_{S,100}$

The average value of S-wave velocity of the uppermost 100 m overlying each borehole station, $V_{S,100}^J$, is estimated from 157 velocity data recorded by stations: C012, C047, C050 and C134. Starting from the MS, we measure 157, 147, 133, 89 and 53 interference frequencies $f_N^{I,J}$, with N from 0 to 4, respectively. The estimates of the difference between adjacent interference

frequencies, $\Delta f_{N,N+1}^J$, are reported in Table 4. The values of $\Delta f_{N,N+1}^J$, spanning from about 1.4 and 1.8 Hz, are characterized by standard errors up to 7%. The largest errors, from 4 to 7%, are obtained with station C127, the smallest, from 3 to 5%, with station C012. For all stations, percentage errors increase with N . Indeed, frequencies corresponding to the highest values of N are generally less readable from the MS. As a consequence, for increasing values of N , Table 4 shows a decreasing number of data used to estimate $\Delta f_{N,N+1}^J$. Table 4 also reports the mean value of the difference between adjacent frequencies, Δf^J , computed for each station as described in Section 4.4 (see also supplementary data). The results evidence the high quality of the estimates of Δf^J performed with stations C012 and C050, and characterized by an error of about 2%. Moreover, it highlights the clear compatibility of these two estimates. For station C127, we estimate a slightly different value of Δf^J with an error of about 3%, while station C047 provides a mean value of Δf^J which is comparable with the estimates obtained for C012 and C050, but with an error of about 3%, reflecting the higher dispersion of the differences $\Delta f_{N,N+1}^J$. The obtained values of $V_{S,100}^J$, reported in Table 4, show the same statistical properties of the measures of Δf^J . We obtain a good compatibility of the estimates of S-wave velocity only for stations: C012, C050 and C047. As an example, the probability that: $|V_{S,100}^{C127} - V_{S,100}^J| > 15$ m/s is: 73, 65, and 94% for stations: C012, C050 and C047, respectively. We choose the reference value of 15 m/s as about twice the estimated standard errors of $V_{S,100}^J$ in order to consider the corresponding S-wave profiles as distinct.

5.3 S-wave velocity and quality factor of the area

Table 3 shows the values of k_0^J estimated with the methods described in Section 4.3. In principle any of them could be used to compute $\Delta k_{0,100}$. However, both theoretical considerations reported in Section 4.3 and regression results (see Section 5.1) lead to the choice of method (D) and to the exclusion of stations C001 and C047 to assess the best estimate of $\Delta k_{0,100}$. In fact, methods (C) and (D) tend to avoid the influence of source and path effects and use more data than methods (A) and (B), thus resulting more efficient in reducing the uncertainty on k_0^J . However, method (D) is the one that best exploits the geometric features of the network. In addition, being interested in an areal estimate of $\Delta k_{0,100}$ and aiming to provide a predictive result for the area, we characterize the uncertainty of $\Delta k_{0,100}$ in terms of standard deviation. Based on these assumptions we obtain: $\Delta k_{0,100} = (11 \pm 3)$ ms (see Table 5 - method A1).

Unlike $\Delta k_{0,100}^J$, $V_{S,100}$ measurements made with single stations are independent of one another (see Sections 4.3 and 4.4). In particular, we find a significant difference between $V_{S,100}^{C127}$ and the corresponding estimates obtained with data from other borehole stations (see

Section 5.2). However, since we are primarily interested in estimating an average value of the quality factor in the investigated area, we calculate $V_{S,100}$ as a weighted mean of the values of $V_{S,100}^J$ estimated with all borehole stations except $V_{S,100}^{C047}$. In fact, this value of the S-wave velocity could be biased due to the use of only the EW component. By considering the standard deviation as uncertainty measure we obtain: $V_{S,100} = (309 \pm 11)$ m/s (see Table 5 - method A1). This value is well inside the range of V_S profiles of Mascandola et al. (2019), based on numerical inversion of 35 ambient-vibration array data collected in a wide part of central and eastern Po Plain (see their Fig. 5a). We thus employ mean and standard deviation of the above-mentioned profiles distribution in order to infer a specific value of depth dependence: $x = 0.3$. Afterwards, we apply eq. (15) to evaluate the range of zero-depth S-wave velocities, $V_{S_0} = (107 \pm 4)$ m/s, and finally, by applying eqs. (13) and (14) we obtain: $Q_{S_0} = 11 \pm 3$ and $Q_{S,100} = 31 \pm 10$ (see Table 5 - method A1).

6 DISCUSSION

6.1 Accuracy of kappa and $V_{S,100}$ estimates

In this section, we point out some issues related to the accuracy of the estimates of kappa and $V_{S,100}$ obtained by means of surface and borehole recordings. Indeed, the use of borehole stations has often been favored because of the generally low levels of noise observed at depth, and the possibility to measure the spectral decay parameter by removing the influence of the shallower sedimentary layers (Ktenidou et al. 2013, 2015; Cabas et al. 2017; Xu et al. 2020). However, unless data have been recorded at sufficiently large depth, the measure of kappa performed with borehole stations can be affected by interference effects between incident and surface-reflected seismic waves. A comprehensive investigation on this aspect is beyond the scope of this work; however, in this section we perform a short test to have a first appraisal of the influence of interference effects on kappa estimation. For this purpose, we take as reference the seismic profile developed in the previous section: $V_S(h) \simeq 107 (1 + h/h_{ref})^{0.3}$ m/s; $Q_S(h) \simeq 11 (1 + h/h_{ref})^{0.3}$, and consider a halfspace velocity of 800 m/s. Fig. 9 (a) deals with the evaluation of kappa when the input motion consists of S-waves with vertical incidence and the halfspace depth of the above-mentioned seismic profile is fixed to 120 m. The input acceleration spectrum is assumed to follow an omega-squared model of an M_L 3.5 earthquake with a kappa value of 59 ms at the top of the halfspace. The corner frequency, $f_c = 2.4$ Hz, is computed as described in Section 4.2. Other spectral parameters, including the crustal Q, which is assumed to have a linear frequency dependence, are not taken into consideration.

Indeed, they only involve a scaling factor on the acceleration spectrum, which is not significant for subsequent analyses. The main panel of Fig. 9 (a) shows the surface and borehole (100 m depth) acceleration spectra together with the areas which encompass the high frequency fits, obtained with f_A values ranging from 5.5 to 8.0 Hz and with $f_B = 20$ Hz. The values of kappa, k^{surf} and k^{bore} , computed by substituting the above-mentioned profile in eq. (7), are 71 and 60 ms, respectively. By definition, both k^{surf} and k^{bore} refer to direct propagation of seismic waves, which in principle does not apply to the spectra shown in the figure. Indeed, the borehole spectrum corresponds to upgoing waves interfering with downgoing waves attenuated by the upper part of the seismic profile. For this reason, the correct value of kappa should be assessed in the highest possible frequency band. The insert of Fig. 9 (a) shows the difference between the kappa values inferred from the slope of the linear regression between f_A and f_B of acceleration spectra and the corresponding theoretical kappa values computed through eq. (7). The insert highlights both a significant variability of the bias, in particular for k^{bore} , and the tendency of the bias toward zero for increasing values of f_A . From the results of this example we generally expect an underestimation of some milliseconds of the kappa values computed through linear regression of the spectra with respect to theoretical ones. We also expect a greater variability of k^{bore} with respect to k^{surf} whereas the estimated values of $\Delta k_{0_{100}}$ should only be slightly affected by interference effects.

Fig. 9 (b) deals with the evaluation of $V_{S,100}$ performed with the method described in Section 4.4. In the figure, we compare the values of $V_{S,100}$ obtained by applying this method to synthetic velocity spectra calculated at 100 m depth, with theoretical $V_{S,100}$ values corresponding to the aforementioned velocity profile extended to a depth varying between 70 and 120 m. Synthetic spectra are computed by adopting the previously mentioned input motion. In principle, given a horizontal stratigraphy with an arbitrary number of layers, each of them characterized by different thickness and velocity, the method provides a correct result only for observation points located in the shallowest layer which, irrespective of its thickness, must be homogeneous. Therefore, Fig. 9 (b) provides an appraisal of the applicability of the method when the position of the recording point with respect to the discontinuity between the hypothesized stratigraphy and the underlying bedrock is not fully known. In the figure, the actual value of $V_{S,100}$ is compared with that derived from the frequencies of the first 5 spectral holes, as is done in this work with the recordings. From a comparison, we can observe that for halfspace depths greater than borehole depths, $V_{S,100}$ is slightly underestimated and shows a significant uncertainty, resulting from non-uniform differences of the adjacent interference frequencies. The figure also shows that, when the borehole station is up to 10-15 m inside the

halfspace, the estimate of $V_{S,100}$ is still acceptable. Thus, this analysis supports the validity of the estimated values of $V_{S,100}$ for the borehole stations reported in Table 4.

6.2 Site-specific kappa and $\Delta k_{0,100}$

In Section 5.1, the site-specific kappa, k_0^J , is estimated for each station of the network, together with $\Delta k_{0,100}^J$, and the slope of the linear increase with distance of the spectral decay parameter, m (or m^J). Note that although for the purpose of this work m is less important than $\Delta k_{0,100}^J$, an unbiased estimation of the former is essential in order to assess the correct value of k_0^J . In this regard, the application of method (A) can be considered as a preliminary analysis of data, with the aim of verifying the hypothesis of a common distance dependence of k for all stations of the network. The results show a moderate variability of m parameter, which supports a reliable application of methods (B), (C) and (D).

As noted earlier, although the k -record values are characterized by a large dispersion with respect to the adopted regression model, both the large number of data and the methods adopted in this work allow us to limit the standard errors of $\Delta k_{0,100}^J$ and k_0^J (see Table 3). Given the main task of this work, namely an accurate estimation of k_0^{surf} and k_0^{bore} , quantifying this effect is particularly important. We investigate this point by considering the residuals between observed and estimated k -record values for the methods described in Section 4.3 and applied in Section 5.1. Fig. 10 shows the distributions of residuals of all stations obtained with all methods. Distributions are computed by taking into account the uncertainties of the residuals, deriving from the k -record measurement errors. The figure highlights that the distributions of residuals obtained with all methods are asymmetrical (skewness is about 0.5), characterized by negative median values (from about -3 to -5 ms) and large dispersion (standard deviations are about 18 ms for methods (A), (B) and (C), and about 16 ms for method (D)). Note that, in the latter case residuals refer to \bar{k}^J , and the estimation of this parameter introduces a preliminary reduction of dispersion of the k -record values. Standard deviations obtained with methods (A), (B) and (C) are than higher compared to the one of method (D). The large number of data employed in the analysis, however, allows reducing the uncertainties of the estimated parameters by about a factor of 4 with respect to the above values of standard deviation. Indeed, for methods (B), (C) and (D), the root-mean-squared errors of the performed regressions are 5, 5 and 4 ms, respectively (see Table 3) and, in the range of distance between 0 and 150 km, the 95% confidence limits provide average uncertainties confined in the ranges: [3, 4] ms; [1, 2] ms and [2, 4] ms, respectively. Minimum values of uncertainty are generally obtained around 70-80 km distance (see Figs. 6 and 7).

Site-specific kappa is estimated with comparable or lower uncertainties. By considering all stations, with methods (B), (C) and (D) we obtain mean standard errors of 2, 1 and 2 ms, respectively (see Table 3). We consider these results as a consequence of the large number of k -record estimates collected around 50-60 km distance, which provides high stability to regressions.

A further confirmation of the stability of the measurements of k_0^J and, consequently, of $\Delta k_{0,100}$ can be obtained by performing some regression tests with non-parametric distance dependence. An example is shown in Fig. 11 where non-parametric and parametric regressions of the average event kappa are compared. It is apparent from the figure that, due to the high density of data around 40-50 km, both mean values and uncertainty intervals of the site-specific kappa do not depend on the adopted type of regression.

Concerning $\Delta k_{0,100}^J$, we can observe from Table 3 that, due to error propagation, standard errors of this parameter obtained with method (B) are generally higher than the corresponding values of $\sigma_{k_0^J}$. Conversely, an opposite trend is evidenced from methods (C) and (D). This can be due to the larger number of data available from selection 2 (see Section 3), and to the direct estimation of $\Delta k_{0,100}^J$ performed with method (C). A straightforward way to investigate the dispersion of $\Delta k_{0,100}^J$ is provided by method (C). Fig. 12 shows the distributions of $\Delta k_{0,100}^J$ obtained with this method for all stations of the network and the corresponding $\Delta k_{0,100}^J$ mean values and standard errors. On average, distributions have standard deviations of about 10 ms. Note that estimating $\Delta k_{0,100}^J$ by this method involves evaluating the difference between k -record values referring to the same earthquake. Therefore, the observed dispersions do not depend on source or path effects and reflect the variability of the k -record values measured at the concerned station and at the reference. Despite this variability, we obtain for $\Delta k_{0,100}$, which represents the high-frequency attenuation of the shallowest 100 m of stratigraphy averaged over the installation area of the network, a 27% coefficient of variation (see Table 5).

It is worth noting that evaluating near-surface attenuation through direct measurement of seismological parameters carried out with surface and borehole data is not so frequent in the literature. Some studies report distributions of site-specific kappa referring to large data-sets of surface and borehole stations, thus only allowing for statistical evaluations of Δk_0 (Oth et al. 2011; Van Houtte et al. 2011). In others, estimates of Δk_0 are performed at individual sites but the results reflect the wide variety of geological conditions which is typical of this kind of study. Also network configurations are heterogeneous, with borehole stations installed at different depth and surface-to-borehole station pairs not aligned along the common vertical (Lai et al. 2016; Pilz & Fäh 2017; Cabas et al. 2017; Xu et al. 2020). As an example,

both Cabas et al. (2017) and Xu et al. (2020) selected data from the Kiban-Kyoshin strong motion network (KiK-net) array in Japan (National Research Institute for Earth Science and Disaster Prevention (NIED) 1996), obtaining direct measures of Δk_0 for 60 and 51 sites, respectively. For comparison purposes, from the studies above we select measures of Δk_0 referred to borehole depths between 100 and 110 m, obtained at sites with $V_{S,30} < 250$ m/s and characterized by S-wave velocities at the borehole depth less than 600 m/s. Only four sites meet these criteria giving site-specific kappa in the range [62, 83] ms at surface and in the range [37, 55] ms in the boreholes (see Xu et al. (2020), Table I, stations: KSRH02; KSRH03; KSRH09; TKCH07). On average, these sites are characterized by $\Delta k_0 = (26 \pm 11)$ ms and thus show high-frequency attenuation higher than that estimated for the area analyzed in this work (see Table 5). These sites being characterized by V_S values comparable with those considered in this paper, we hypothesize that the higher attenuation estimated with Δk_0 by Xu et al. (2020) is due to a different lithology (see Zhu et al. (2020)) and a different contribution of the scattering mechanism. This latter phenomenon, as pointed out by Ktenidou et al. (2015), can be enhanced by the likely higher degree of heterogeneity in the stratigraphies of the examined Kik-net sites.

6.3 S-wave velocity in the upper 100 m and S-wave quality factor of the area

In Section 5.2, the S-wave velocity in the upper 100 m of stratigraphy is estimated from measurements of the frequency difference between two adjacent interference frequencies, observed on the velocity MS of borehole data. Single-station estimates of this quantity, $V_{S,100}^J$, are independent of each other, and the obtained results show a good agreement between the $V_{S,100}^J$ values of stations C012, C050 and C047, with a mean value of 300 m/s and maximum standard errors of about 3% (see Table 4). Station C127 shows an 8% higher value of S-wave velocity and a comparable standard error. The measured uncertainties assure that $V_{S,100}^{C127}$ is significantly different with respect to the values of $V_{S,100}^J$ obtained at the other borehole stations (see Section 5.2). Indeed, the installation site of C127 was slightly decentralized with respect to the other boreholes and, by considering the previously mentioned geological unconformity named as Y-surface (see Section 2), we can hypothesize that data recorded by station C127 could be partially affected by the proximity of this surface (see Fig. 1). In Section 2 we noticed that the Y-surface gradually deepens when moving from SSW to NNE. Due to uncertainties related to the estimated depth of this surface, we can hypothesize that station C127 was installed slightly beneath this unconformity. In this case, we should measure a value of $V_{S,100}^{C127}$ higher than the velocities observed at the other borehole stations. Section 6.1 shows the results

obtained from numerical simulations concerning this point. The simulations, performed with values of geotechnical parameters compatible with the characteristics of the area, show that the above values of S-wave velocities can be confidently measured with the methods employed in this work even if with large errors (see Fig. 9 (b)). We believe that the above arguments can explain the mentioned disagreement between $V_{S,100}^{C127}$ and the $V_{S,100}^J$ values obtained with the other borehole stations. In order to estimate an average value of $V_{S,100}$ for the whole area, however, we also consider $V_{S,100}^{C127}$ and, characterizing the uncertainty of this parameter in terms of standard deviation, we obtain a 4% coefficient of variation.

Finally, we estimate $Q_{S,100}$ through eqs. (13), (14) and (15) by adopting the results of Mascandola et al. (2019). The area we are dealing with is in fact well-represented by the aforementioned study and, as shown in Section 5.3, the confidence interval of our $V_{S,100}$ estimate, is well inside the range of variation of the $V_{S,H}$ values that can be inferred from the same paper. In applying the equations above, we also hypothesize $Q_S(h)/V_S(h)$ independent of h . Measurements of quality factor and S-wave velocity for sedimentary deposits are indeed generally characterized by large dispersion but, on average, they show increasing values of Q_S for increasing V_S (see Campbell (2009)). Aiming to provide a rough estimate of the quality factor of the area, we also adopt the simplest possible model to constrain the depth dependence of the quality factor. With the above assumptions we obtain a value of $Q_{S,100}$ which is characterized by a 32% coefficient of variation (see Table 5 - method A1). Similar results are obtained by considering the velocity interval between the extreme values of $V_{S,100} \pm \sigma_{V_{S,100}}$ (see Table 4, columns $V_{S,100}$ and $\sigma_{V_{S,100}}$ with the exception of C047). Applying eq. (15) with $x = 0.3$, we extrapolate these limits to 30 m and evaluate the corresponding values of Q_S taking into account a constant Q_S/V_S ratio. Since our network has no co-located surface/borehole stations, the ratio is assessed as $Q_S/V_S = H/(\Delta k_{0H} \cdot V_{S,H}^2)$, employing the mean values of Δk_{0100} and $V_{S,100}$. We then obtain minimum and maximum values of $Q_{S,100}$ given by: $Q_{S,100}^{min} = 19$ and $Q_{S,100}^{max} = 40$, respectively (see Table 5 - method A2).

The results obtained with methods A1 and A2 are compared in Fig. 13 (a) together with average values of V_S and Q_S estimated by Boore et al. (2020), who estimated these parameters by averaging them over depth ranges from about 8 to 70 m. For comparison purposes, we consider only borehole data characterized by fine- to medium-grained lithologies, collected in the San Francisco Bay area and in the San Fernando Valley. Considering that our data refer to slightly deeper boreholes than those shown in the above work, the figure shows the compatibility between the estimates of V_S and Q_S obtained in these two papers. Note that, in case of lack of information regarding the velocity profile, Q_S can still be approximately

evaluated by replacing eq. (13) with: $\Delta k_{0_H} = H / (Q_{S,H} \cdot V_{S,H})$. In such case, we obtain: $Q_{S,100} = 28 \pm 9$ (see Table 5 - method A3).

Information about the velocity profile, however, also makes it possible to compute the time-averaged S-wave velocity and S-wave quality factor referred to the standard depth of 30 m, and thus comparing the estimated values with existing scientific literature. Recent measurements of both $V_{S,30}$ and $Q_{S,30}$ are reported by Boxberger et al. (2017). In Fig. 13 (b) our values of $V_{S,30}$ and $Q_{S,30}$, computed according to methods A1 and A2 (see Table 5), are compared with the estimates of Boxberger et al. (2017) obtained with data collected in different geological environments of Europe and Central Asia. For comparison purposes we consider array data of sandy and clayey lithologies. The figure shows a general agreement between our estimates of $V_{S,30}$ and $Q_{S,30}$ and the distributions of the same parameters obtained by Boxberger et al. (2017). As an example, according to method A1, the 68% confidence interval of the difference between the estimated value of $V_{S,30}$ and the corresponding mean value of the distribution of $V_{S,30}$ of the clayey lithologies is: (13 ± 35) m/s. For $Q_{S,30}$ the analogous interval is: 10 ± 10 . Therefore, our measurements of Q_S and V_S can be meaningful also for other sites characterized by fine- to medium-grained lithologies such as those located in a wide part of the Po Plain (northern Italy).

7 CONCLUSIONS

We used velocity data recorded by a microseismic network consisting of both surface and borehole sensors which sampled an almost uniform lithological condition in the central Po Plain (northern Italy), with the aim of performing field measurements of S-wave attenuation in the uppermost 100 m of surface deposits. Several results can be highlighted:

1) The four different strategies used to compute $\Delta k_{0_{100}}$, the difference between the values of k estimated at the surface and at the boreholes depth, respectively, are in good agreement. In particular, a method which exploits the small network dimensions with respect to event distances provides $\Delta k_{0_{100}} = (11 \pm 3)$ ms. With the same method we obtain k_0 values between 64 and 68 ms for borehole stations and between 75 and 79 ms for surface stations, with a maximum standard error of about 3%. Moreover, all methods suggest for m , the slope of the linear increase of k with distance, a value ranging from 0.07 and 0.08 ms/km.

2) Accurate measurements of interference frequencies observed at borehole stations in the low-frequency portion of the amplitude velocity spectra, allowed computing $V_{S,100}^J$, the time-averaged S-wave velocity of the 100 m stratigraphy overlying each borehole station. We obtain

a good compatibility of the estimates of $V_{S,100}^J$ for stations C012, C050 and C047, with a mean value of 300 m/s and maximum standard errors of about 3%. The remaining borehole station, C127, shows an 8% higher value of $V_{S,100}^J$ with a comparable standard error. Based on numerical simulations, we suggest that the observed disagreement between $V_{S,100}^{C127}$ and $V_{S,100}^J$ values from the other borehole stations could be explained by considering the proximity of C127 to a recognized geologic unconformity mapped in this area (Martelli et al. 2017). On average, the time-averaged S-wave velocity of the uppermost 100 m of the area is $V_{S,100} = (309 \pm 11)$ m/s. This value is well within the range of V_S profiles inferred from array data collected over a large portion of the central and eastern Po Plain (Mascandola et al. 2019).

3) The best estimate of $Q_{S,100}$, computed by using the above estimates of $\Delta k_{0,100}$ and $V_{S,100}$, and a specific depth dependence of V_S and Q_S , is: $Q_{S,100} = 31 \pm 10$. In the case of V_S and Q_S independent of depth we obtain: $Q_{S,100} = 28 \pm 9$. Both these estimates of $Q_{S,100}$ and those of $V_{S,100}$ show a good compatibility with the results of Boore et al. (2020) concerning S-wave velocities and quality factors inferred from borehole data characterized by fine- to medium-grained lithologies, collected in the San Francisco Bay area and in the San Fernando Valley.

4) Using the previously mentioned depth dependence of V_S and Q_S , from the above estimates of $V_{S,100}$ and $Q_{S,100}$ we infer: $V_{S,30} = (224 \pm 8)$ m/s and $Q_{S,30} = 23 \pm 7$. These values are in agreement with the results of Boxberger et al. (2017) obtained from data characterized by clayey lithologies, collected at several sites in Europe and Central Asia.

The above results confirm that microseismic networks consisting of both surface and borehole stations are relevant for inferring near-surface attenuation properties of seismic waves, even for sites where the S-wave velocity profile is unknown. In fact, using a sufficient number of earthquake data recorded by these networks, it is possible to apply appropriate methodologies in order to reduce the uncertainties in the estimated parameters, despite the large scatter that k -record values show on the distance-dependence model. Moreover, accurate measures of both k -record and interference frequencies, which can be observed in earthquakes spectra of velocity data recorded at depth, allow inferring reliable values of both V_S and Q_S , averaged over a vertical profile that extends to the boreholes depth. In this work, we estimate near-surface attenuation properties in the field, thus accounting for both intrinsic and scattering attenuation. Therefore, our results could be significant for site-response predictions at other sites located in large alluvial basins, where lithostatic pressure is the main factor controlling the rigidity of fine- to medium-grained sedimentary layers.

ACKNOWLEDGMENTS

We would like to thank Paolo Augliera (Istituto Nazionale di Geofisica e Vulcanologia) and Snam-Stogit S.p.A. for their collaboration during the management of the microseismic network. This study received financial support from “Comune di Minerbio” under the grant “Sperimentazione ILG Minerbio” (grant number 0913.010).

DATA AVAILABILITY AND RESOURCES

Information on historical seismicity is available in the Parametric Catalogue of Italian Earthquakes (<https://emidius.mi.ingv.it/CPTI15-DBMI15/>; Rovida et al. 2022).

Instrumental seismicity data are taken from the Italian Seismological Instrumental and Parametric Data-Base (<http://terremoti.ingv.it/iside>; ISIDE Working Group 2007) managed by the Italian National Earthquake Observatory (<https://www.ont.ingv.it/>).

Information on the microseismic network instruments can be found in the Lennartz Electronic website (<https://www.lennartz-electronic.de/>).

V_S profiles of the Kiban-Kyoshin strong-motion network (KiK-net) stations are available in the website of the NIED strong-motion seismograph networks (<https://www.kyoshin.bosai.go.jp/>).

The software adopted for the analysis are:

SAC (<https://ds.iris.edu/ds/nodes/dmc/software/downloads/sac/>;

IRIS - Incorporated Research Institutions for Seismology 2013);

Octave (<https://octave.org/>; Eaton et al. 2020) and

GMT (<https://www.generic-mapping-tools.org/>; Wessel et al. 2013).

The waveform data underlying this article are from a third party (Snam-Stogit S.p.A.) and the authors do not have permission to distribute them.

All websites were last accessed in December 2022.

REFERENCES

- Al Atik, L., Kottke, A., Abrahamson, N. & Hollenback, J., 2014. Kappa (k) Scaling of Ground-Motion Prediction Equations Using an Inverse Random Vibration Theory Approach, *Bull. seism. Soc. Am.*, **104**(1), 336–346.
- Anderson, J. G., 1991. A Preliminary Descriptive Model for the Distance Dependence of the Spectral Decay Parameter in Southern California, *Bull. seism. Soc. Am.*, **81**(6), 2186–2193.
- Anderson, J. G. & Hough, S. E., 1984. A Model for the Shape of the Fourier Amplitude Spectrum of Acceleration at High Frequencies, *Bull. seism. Soc. Am.*, **74**(5), 1969–1993.

- Augliera, P., Franceschina, G., Lovati, S., Massa, M., D'Alema, E., Marzorati, S., Marchesi, E. & Marzorati, D., 2012. Seismic Monitoring of CO₂ Geo-sequestration in Italy: Analysis of Signals from a 6-Km Aperture Seismic Array, *European Seismological Commission, 33rd General Assembly*, 19-24 August 2012, Moscow, Russia, **Book of Abstracts**, 236.
- Bigi, G., Bonardi, G., Catalano, R., Cosentino, D., Lentini, F., Parotto, M., Sartori, R., Scandone, P. & Turco, E. (eds.), 1992. Structural Model of Italy 1:500,000, Sheet 1, *CNR - Progetto Finalizzato Geodinamica*, SELCA, Firenze, Italy.
- Bindi, D., Castro, R. R., Franceschina, G., Luzi, L. & Pacor, F., 2004. The 1997–1998 Umbria-Marche sequence (central Italy): Source, path, and site effects estimated from strong motion data recorded in the epicentral area, *J. geophys. Res.*, **109**(B4), B04312.
- Boore, D. M., 2003. Simulation of Ground Motion Using the Stochastic Method, *Pure appl. Geophys.*, **160**(3), 635–676.
- Boore, D. M., Gibbs, J. F. & Joyner, W. B., 2020. Damping Values Derived from Surface-Source, Downhole-Receiver Measurements at 22 Sites in the San Francisco Bay Area of Central California and the San Fernando Valley of Southern California, *Bull. seism. Soc. Am.*, **111**(4), 2158–2166.
- Boxberger, T., Pilz, M. & Parolai, S., 2017. Shear wave velocity versus quality factor: results from seismic noise recordings, *Geophys. J. Int.*, **210**(2), 660–670.
- Cabas, A. & Rodriguez-Marek, A., 2017. $V_S - k_0$ Correction Factors for Input Ground Motions Used in Seismic Site Response Analyses, *Earthq. Spectra*, **33**(3), 917–941.
- Cabas, A., Rodriguez-Marek, A. & Bonilla, L. F., 2017. Estimation of Site-Specific Kappa (k_0)-Consistent Damping Values at KiK-Net Sites to Assess the Discrepancy between Laboratory-Based Damping Models and Observed Attenuation (of Seismic Waves) in the Field, *Bull. seism. Soc. Am.*, **107**(5), 2258–2271.
- Calderoni, G., Rovelli, A. & Singh, S. K., 2013. Stress drop and source scaling of the 2009 April L'Aquila earthquakes, *Geophys. J. Int.*, **192**(1), 260–274.
- Campbell, K. W., 2009. Estimates of Shear-Wave Q and k_0 for Unconsolidated and Semiconsolidated Sediments in Eastern North America, *Bull. seism. Soc. Am.*, **99**(4), 2365–2392.
- Carminati, E. & Doglioni, C., 2012. Alps vs. Apennines: The paradigm of a tectonically asymmetric Earth, *Earth-Science Reviews*, **112**, 67–96.
- Castro, R. R., Condori, C., Romero, O., Jacques, C. & Suter, M., 2008. Seismic Attenuation in Northeastern Sonora, Mexico, *Bull. seism. Soc. Am.*, **98**(2), 722–732.
- Castro, R. R., Pacor, F., Puglia, R., Ameri, G., Letort, J., Massa, M. & Luzi, L., 2013. The 2012 May 20 and 29, Emilia earthquakes (Northern Italy) and the main aftershocks: S-wave attenuation, acceleration source functions and site effects, *Geophys. J. Int.*, **195**(1), 597–611.
- Castro, R. R., Singh, S. K., Joshi, A. & Singh, S., 2019. Shear-Wave Attenuation Study in the South Region of the Gulf of California, Mexico, *Bull. seism. Soc. Am.*, **109**(2), 600–609.
- Douglas, J., Gehl, P., Bonilla, L. & Gélis, C., 2010. A k model for mainland France, *Pure appl.*

Geophys., **167**, 1303–1315.

- Eaton, J. W., Bateman, D., Hauberg, S. & Wehbring, R., 2020. GNU Octave version 6.1.0 manual: a high-level interactive language for numerical computations, <https://docs.octave.org/v6.1.0/>.
- Edwards, B., Michel, C., Poggi, V. & Fäh, D., 2013. Determination of Site Amplification from Regional Seismicity: Application to the Swiss National Seismic Networks, *Seismol. Res. Lett.*, **84**(4), 611–621.
- Fantoni, R. & Franciosi, R., 2010. Tectono-sedimentary setting of the Po Plain and Adriatic Foreland, *Rend. Fis. Acc. Lincei*, **21** (Suppl 1), S197–S209.
- Fernández, A. I., Castro, R. R. & Huerta, C. I., 2010. The Spectral Decay Parameter Kappa in Northeastern Sonora, Mexico, *Bull. seism. Soc. Am.*, **100**(1), 196–206.
- Franceschina, G., Kravanja, S. & Bressan, G., 2006. Source parameters and scaling relationships in the Friuli-Venezia Giulia (Northeastern Italy) region, *Phys. Earth planet. Inter.*, **154**(2), 148 – 167.
- Franceschina, G., Gentili, S. & Bressan, G., 2013. Source parameters scaling of the 2004 Kobarid (Western Slovenia) seismic sequence, *Phys. Earth planet. Inter.*, **222**, 58 – 75.
- Franceschina, G., Augliera, P., Lovati, S. & Massa, M., 2015. Surface seismic monitoring of a natural gas storage reservoir in the Po Plain (northern Italy), *Boll. Geofis. Teor. Appl.*, **56**(4), 489–504.
- Gentili, S. & Franceschina, G., 2011. High frequency attenuation of shear waves in the southeastern Alps and northern Dinarides, *Geophys. J. Int.*, **185**(3), 1393–1416.
- Hough, S. E., Anderson, J. G., Brune, J., Vernon, F., I., Berger, J., Fletcher, J., Haar, L., Hanks, L. & Baker, L., 1988. Attenuation near Anza, California, *Bull. seism. Soc. Am.*, **78**(2), 672–691.
- Ibs-von Seht, M. & Wohlenberg, J., 1999. Microtremor Measurements Used to Map Thickness of Soft Sediments, *Bull. seism. Soc. Am.*, **89**(1), 250–259.
- IRIS - Incorporated Research Institutions for Seismology, 2013. SAC (Seismic Analysis Code), Users Manual, Version 101.6a, http://www.adc1.iris.edu/files/sac-manual/sac_manual.pdf.
- ISIDe Working Group, 2007. Italian Seismological Instrumental and Parametric Database (ISIDe), Istituto Nazionale di Geofisica e Vulcanologia (INGV), <https://doi.org/10.13127/ISIDE>.
- Knopoff, L., 1964. Q , *Rev. Geophys.*, **2**(4), 625–660.
- Kramer, S. L., 1996. *Geotechnical Earthquake Engineering*, Prentice-Hall International Series in Civil Engineering and Engineering Mechanics, Prentice-Hall, Upper Saddle River, NJ, 653 pp.
- Ktenidou, O. & Abrahamson, N. A., 2016. Empirical Estimation of High-Frequency Ground Motion on Hard Rock, *Seismol. Res. Lett.*, **87**(6), 1465–1478.
- Ktenidou, O., Gélis, C. & Bonilla, L., 2013. A Study on the Variability of Kappa (k) in a Borehole: Implications of the Computation Process, *Bull. seism. Soc. Am.*, **103**(2A), 1048–1068.
- Ktenidou, O., Cotton, F., Abrahamson, N. A. & Anderson, J. G., 2014. Taxonomy of k : A Review of Definitions and Estimation Approaches Targeted to Applications, *Seismol. Res. Lett.*, **85**(1), 135–146.
- Ktenidou, O.-J., Abrahamson, N. A., Drouet, S. & Cotton, F., 2015. Understanding the physics of kappa (k): insights from a downhole array, *Geophys. J. Int.*, **203**(1), 678–691.

- Lai, T., Mittal, H., Chao, W. & Wu, Y., 2016. A Study on Kappa Value in Taiwan Using Borehole and Surface Seismic Array, *Bull. seism. Soc. Am.*, **106**(4), 1509–1517.
- Laurendeau, A., Cotton, F., Ktenidou, O., Bonilla, L. & Hollender, F., 2013. Rock and Stiff-Soil Site Amplification: Dependency on V_{S30} and Kappa (k_0), *Bull. seism. Soc. Am.*, **103**(6), 3131–3148.
- Laurenzano, G., Priolo, E., Mucciarelli, M., Martelli, L. & Romanelli, M., 2017. Site response estimation at mirandola by virtual reference station, *Bull. Earthq. Eng.*, **15**(6), 2393–2409.
- Li, J., Zhou, B., Rong, M., Chen, S. & Zhou, Y., 2020. Estimation of Source Spectra, Attenuation, and Site Responses from Strong-Motion Data Recorded in the 2019 Changning Earthquake Sequence, *Bull. seism. Soc. Am.*, **110**(2), 410–426.
- Malagnini, L. & Munafò, I., 2018. On the Relationship between M_L and M_w in a Broad Range: An Example from the Apennines, Italy, *Bull. seism. Soc. Am.*, **108**(2), 1018–1024.
- Malagnini, L., Scognamiglio, L., Mercuri, A., Akinci, A. & Mayeda, K., 2008. Strong evidence for non-similar earthquake source scaling in central Italy, *Geophys. Res. Lett.*, **35**(17).
- Martelli, L., Bonini, M., Calabrese, L., Corti, G., Ercolessi, G., Molinari, F. C., Piccardi, L., Pondrelli, S., Sani, F. & Severi, P., 2017. Carta sismotettonica della Regione Emilia-Romagna, scala 1:250.000. Note illustrative, *Regione Emilia-Romagna-SGSS, CNR-IGG, SELCA, Firenze*.
- Mascandola, C., Massa, M., Barani, S., Albarello, D., Lovati, S., Martelli, L., & Poggi, V., 2019. Mapping the Seismic Bedrock of the Po Plain (Italy) through Ambient-Vibration Monitoring, *Bull. seism. Soc. Am.*, **109**(1), 164–177.
- Mayor, J., Bora, S. S. & Cotton, F., 2018. Capturing Regional Variations of Hard-Rock k_0 from Coda Analysis, *Bull. seism. Soc. Am.*, **108**(1), 399–408.
- Motazedian, D. & Atkinson, G. M., 2005. Stochastic Finite-Fault Modeling Based on a Dynamic Corner Frequency, *Bull. seism. Soc. Am.*, **95**(3), 995–1010.
- National Research Institute for Earth Science and Disaster Prevention (NIED), 1996. Strong Motion Seismograph Networks (K-NET, KiK-net), <http://www.kyoshin.bosai.go.jp/>.
- Oth, A., Bindi, D., Parolai, S. & Di Giacomo, D., 2011. Spectral Analysis of K-NET and KiK-net Data in Japan, Part II: On Attenuation Characteristics, Source Spectra, and Site Response of Borehole and Surface Stations, *Bull. seism. Soc. Am.*, **101**(2), 667–687.
- Pacor, F., Spallarossa, D., Oth, A., Luzi, L., Puglia, R., Cantore, L., Mercuri, A., D’Amico, M. & Bindi, D., 2016. Spectral models for ground motion prediction in the L’Aquila region (central Italy): evidence for stress-drop dependence on magnitude and depth, *Geophys. J. Int.*, **204**(2), 697–718.
- Paolucci, E., Albarello, D., D’Amico, S., Lunedei, E., Martelli, L., Mucciarelli, M. & Pileggi, D., 2015. A large scale ambient vibration survey in the area damaged by May–June 2012 seismic sequence in Emilia Romagna, Italy, *Bull. Earthq. Eng.*, **13**(11), 3187–3206.
- Paolucci, R., Mazzieri, I., Smerzini, C. & Stupazzini, M., 2014. Physics-Based Earthquake Ground Shaking Scenarios in Large Urban Areas, in *Perspectives on European Earthquake Engineering and Seismology - Volume 1*, pp. 331–359, ed. Ansal, A., Springer International Publishing, Cham.

- Parolai, S. & Bindi, D., 2004. Influence of Soil-Layer Properties on k Evaluation, *Bull. seism. Soc. Am.*, **94**(1), 349–356.
- Parolai, S., Lai, C. G., Dreossi, I., Ktenidou, O.-J. & Yong, A., 2022. A review of near-surface Q_S estimation methods using active and passive sources, *J. Seismol.*, **26**, 823–862.
- Perron, V., Hollender, F., Bard, P., Gélis, C., Guyonnet-Benaize, C., Hernandez, B. & Ktenidou, O., 2017. Robustness of Kappa (k) Measurement in Low-to-Moderate Seismicity Areas: Insight from a Site-Specific Study in Provence, France, *Bull. seism. Soc. Am.*, **107**(5), 2272–2292.
- Pilz, M. & Fäh, D., 2017. The contribution of scattering to near-surface attenuation, *J. Seismol.*, **21**, 837–855.
- Rodriguez-Marek, A., Rathje, E. M., Bommer, J. J., Scherbaum, F. & Stafford, P. J., 2014. Application of Single-Station Sigma and Site-Response Characterization in a Probabilistic Seismic-Hazard Analysis for a New Nuclear Site, *Bull. seism. Soc. Am.*, **104**(4), 1601–1619.
- Rovida, A., Locati, M., Camassi, R., Lolli, B., Gasperini, P. & Antonucci, A., 2022. Italian Parametric Earthquake Catalogue CPTI15, version 4.0, https://emidius.mi.ingv.it/CPTI15-DBMI15/data/CPTI15_v4.0_description.pdf.
- Scardia, G., De Franco, R., Muttoni, G., Rogledi, S., Caielli, G., Carcano, C., Sciunnach, D. & Piccin, A., 2012. Stratigraphic evidence of a Middle Pleistocene climate-driven flexural uplift in the Alps, *Tectonics*, **31**(6).
- Shoja-Taheri, J. & Bolt, B. A., 1977. A Generalized Strong-Motion Accelerogram Based on Spectral Maximization from two Horizontal Components, *Bull. seism. Soc. Am.*, **67**(3), 863–876.
- Steidl, J. H., Tumarkin, A. G. & Archuleta, R. J., 1996. What Is a Reference Site ?, *Bull. seism. Soc. Am.*, **86**(6), 1733–1748.
- Tucker, B. E., King, J. L., Hatzfeld, D. & Nersesov, I. L., 1984. Observations of Hard-Rock Site Effects, *Bull. seism. Soc. Am.*, **74**(1), 121–136.
- Tumarkin, A. G. & Archuleta, R. J., 1997. Recent Advances in Prediction and Processing of Strong Ground Motions, *Nat. Hazards*, **15**(2), 199–215.
- Van Houtte, C., Drouet, S. & Cotton, F., 2011. Analysis of the Origins of k (Kappa) to Compute Hard Rock to Rock Adjustment Factors for GMPEs, *Bull. seism. Soc. Am.*, **101**(6), 2926–2941.
- Wessel, P., Smith, W. H. F., Scharroo, R., Luis, J. & Wobbe, F., 2013. Generic Mapping Tools: Improved Version Released, *EOS Trans. AGU*, **94**(45), 409–410.
- Xu, B., Rathje, E. M., Hashash, Y., Stewart, J., Campbell, K. & Silva, W. J., 2020. k_0 for soil sites: Observations from KiK-net sites and their use in constraining small-strain damping profiles for site response analysis, *Earthq. Spectra*, **36**(1), 111 – 137.
- Zhu, C., Weatherill, G., Cotton, F., Pilz, M., Kwak, D. Y. & Kawase, H., 2020. An Open-Source Site Database of Strong-Motion Stations in Japan: K-NET and KiK-net, V.1.0.0, GFZ Data Services, <https://doi.org/10.5880/GFZ.2.1.2020.006>.

FIGURE AND TABLE CAPTIONS

Figure 1. Study area and network configuration. Main panel: location of the microseismic network (dark green box) and epicenters of the selected earthquakes. Circles: earthquakes with $1.3 \leq M_L \leq 4.9$ (symbol dimensions are proportional to earthquake magnitude). Yellow, orange, and red symbols correspond to shallow ($h \leq 10$ km), intermediate ($10 \text{ km} < h \leq 25$ km) and deep ($h > 25$ km) events, respectively. Upper panel: microseismic network with location of surface and borehole instruments (green triangles and brown squares, respectively). The values shown under station labels indicate the instrument elevation with respect to sea level. Labelled dashed lines represent the isohypses of the *Y*-surface (see text). Main communication facilities of the area are also drawn (orange and yellow lines: highways and roads, respectively; black lines: railways).

Figure 2. Upper graph: distribution of local magnitude with respect to epicentral distance of velocity data of selection 1 (crosses) and of velocity data of deep ($h > 25$ km) events (grey circles). Lower graph: as in the upper graph, but for the depth. Epicentral distance is measured from the center of the network.

Figure 3. Horizontal-to-Vertical Spectral Ratios (HVSR) from microtremors recorded at surface stations: the inner panel shows a detail of the frequency range: 0-2 Hz. Thick black line: station C001; thin black line: station C073; grey line: station C134. Spectral ratios are computed using velocity data recorded in continuous mode.

Figure 4. Example of *k*-record estimation: 7 July 2011 $M_L=1.9$ earthquake, recorded by stations C073 (surface) and C012 (borehole). R_e^C is the epicentral distance measured from the center of the network. *h* is depth. (a): velocity records (vertical, NS and EW components) and time windows used for noise and signal analysis (grey areas). (b): *k*-record estimates and standard deviations as a function of the lower limit of the frequency band adopted for the linear regression, f_A (solid and dashed lines, respectively). The adopted values of f_A and f_B are also indicated, and the vertical segment marks the chosen value of f_A . (c): signal and noise maximized acceleration spectra and linear regressions used to obtain the *k*-record estimate. Grey lines: original spectra of signal and noise; black thin line: smoothed noise spectrum; highlighted black thin line: smoothed signal spectrum; black thick line: linear regression. Signal-to-noise ratios, s/n , and *k*-record estimates are also indicated.

Figure 5. Example of interference frequencies estimation: 12 April 2012 $M_L=2.5$ earthquake,

recorded at 26.5 km epicentral distance by station C050. Grey lines: original maximized velocity spectra of signal and noise; black thick and thin lines: smoothed maximized velocity spectrum of signal and noise, respectively; grey areas: measurement errors of the interference frequencies: f_N , $N = 0, 4$.

Figure 6. Functions $k(R_e)$ and corresponding 95% confidence limits, estimated with methods (A) (dashed lines) and (B) (solid line and grey area) for the 7 stations of the microseismic network. Circles with error bars represent the k -record estimates.

Figure 7. Left panels: method (C). Function $k(R_e)$ and corresponding 95% confidence limits estimated for the reference station C012 (black line and grey area, respectively). (C1): for each station J (blue: surface data; red: borehole data) circles with error bars represent the k -record minus $\Delta k_{0.100}^J$ values. (C2): blue and red lines represent the functions $k(R_e)$ obtained for surface and borehole stations, respectively; blue and red labels indicate the regression lines obtained for stations C001 and C047, respectively. Right panels: method (D). Function $k(R_e)$ and corresponding 95% confidence limits estimated for the average event k (black line and grey area, respectively). Epicentral distance is measured from the center of the network. (D1): circles with error bars represent the values of the average event k . (D2): blue and red lines represent the functions $k(R_e)$ obtained for surface and borehole stations, respectively; blue and red labels indicate the regression lines obtained for stations C001 and C047, respectively.

Figure 8. Upper panel: mean slope and corresponding ± 1 standard error of the linear regressions obtained for the 7 stations of the microseismic network with methods (A) (open circles), (B) (closed circles), (C) (squares) and (D) (triangles). Middle panel: as for the upper panel but for site-specific kappa. Lower panel: as for the upper panel but for the difference between the site-specific kappa estimated at each station and that of the reference station (C012).

Figure 9. (a) estimation of k with stratigraphy characterized by wave velocity and quality factor gradually increasing with depth (see text for details). Main panel: surface acceleration spectrum and corresponding area enclosing the straight lines obtained from linear regressions with f_A ranging from 5.5 to 8.0 Hz and $f_B = 20$ Hz (black lines); borehole (100 m depth) acceleration spectrum and corresponding area enclosing the straight lines obtained from linear regressions with the same values of f_A and f_B (grey lines). The simulated acceleration spectra correspond to k values of 60 and 71 ms at 100 m depth and at surface, respectively (see text for details). Inset: k -bias corresponding to the linear regressions shown in the main panel. (b)

estimation of $V_{S,100}$ for different values of bedrock depth (H) and stratigraphy characterized by wave velocity and quality factor gradually increasing with depth (see text for details). Grey symbols: simulated values; black symbols: values of $V_{S,100}$ and corresponding uncertainties, estimated with the method described in Section 4.4.

Figure 10. Distributions of the weighted residuals between observed and predicted k -record values obtained with the methods described in Section 4.3. Distributions are computed by considering the uncertainties of the k -record values (see Section 4.2).

Figure 11. Function $k(R_e)$ and corresponding 95% confidence limits, estimated for the average event k with a non-parametric regression on epicentral distance (red lines) compared with the corresponding curves obtained with method (D) (blue lines). Circles with error bars represent the values of the average event k . Epicentral distance is measured from the center of the network.

Figure 12. Distributions of Δk_{0100}^J obtained for stations: C001, C047, C050, C073, C127 and C134, using method (C). For each station, Δk_{0100}^J is referred to the station C012. Mean values and corresponding standard error intervals are also indicated (vertical black lines).

Figure 13. (a) Time-averaged S-wave velocity and quality factor at 100 m depth computed in this work, compared with the estimates of Boore et al. (2020). Black symbol with error bars: values of $V_{S,100}$ and $Q_{S,100}$ obtained with method A1; grey area: values of $V_{S,100}$ and $Q_{S,100}$ obtained with method A2; grey symbols with error bars: S-wave velocities and quality factors averaged over a depth range from about 8 to 70 m, estimated by Boore et al. (2020) with borehole data collected in the San Francisco Bay area and in the San Fernando Valley characterized by fine- to medium-grained lithologies. (b) Time-averaged S-wave velocity and quality factor at 30 m depth computed in this work, compared with the estimates of the same parameters obtained by Boxberger et al. (2017). Black symbol with error bars: values of $V_{S,30}$ and $Q_{S,30}$ obtained with method A1; grey area: values of $V_{S,30}$ and $Q_{S,30}$ obtained with method A2; grey circles and black triangles: values of $V_{S,30}$ and $Q_{S,30}$ obtained by Boxberger et al. (2017) with data collected in Europe and Central Asia characterized by clayey and sandy lithologies, respectively.

Table 1. Seismic station characteristics.

Table 2. Percentiles, p , of parameter distributions used to estimate k -record: time window duration, T_d ; frequency limits of the least square regression, f_A and f_B ; frequency bandwidth of the least square regression, $f_B - f_A$; difference between the first limit of the least square regression, f_A , and the corner frequency of the event, f_c , estimated through an appropriate scaling with the local magnitude (see text); signal-to-noise ratio, s/n .

Table 3. Slope of the linear trend of k with epicentral distance (m), site-specific kappa (k_0) and difference between the site-specific kappa estimated at each station and that of the reference station (Δk_{0100}) obtained with methods (A), (B), (C) and (D) for the stations of the microseismic network. σ_m ; σ_{k_0} and $\sigma_{\Delta k_{0100}}$ are the standard errors of m , k_0 and Δk_{0100} , respectively. e_k is the root-mean-squared error of the regression. N_k and $N_{\Delta k}$ are the number of data employed to estimate the parameters of $k(R_e)$ and Δk_{0100} , respectively. An asterisk next to the method label indicates that k -record estimates of stations C001 and C047 have been excluded from the computation of the parameters reported in the table.

Table 4. Differences between adjacent interference frequencies and time-averaged S-wave velocity of the uppermost 100 m estimated with the borehole stations. The differences $\Delta f_{N,N+1}$ estimated with frequencies f_N ($N = 0, 4$); the corresponding weighted mean, Δf , and the corresponding time-averaged S-wave velocity, $V_{S,100}$, are reported. $\sigma_{\Delta f_{N,N+1}}$, $\sigma_{\Delta f}$ and $\sigma_{V_{S,100}}$ are the standard errors. M_N is the number of data used to compute f_N .

Table 5. Site specific parameters referring to the installation area of the network, estimated with methods A1, A2 and A3 (see text): difference between the values of k estimated at the surface and at the boreholes depth (Δk_{0100}); time-averaged S-wave velocity and quality factor of the uppermost 100 m ($V_{S,100}$ and $Q_{S,100}$, respectively); time-averaged S-wave velocity and quality factor of the uppermost 30 m ($V_{S,30}$ and $Q_{S,30}$, respectively). For methods A1 and A3, the results are expressed in terms of mean value and standard deviation, for method A2 in terms of minimum and maximum values.

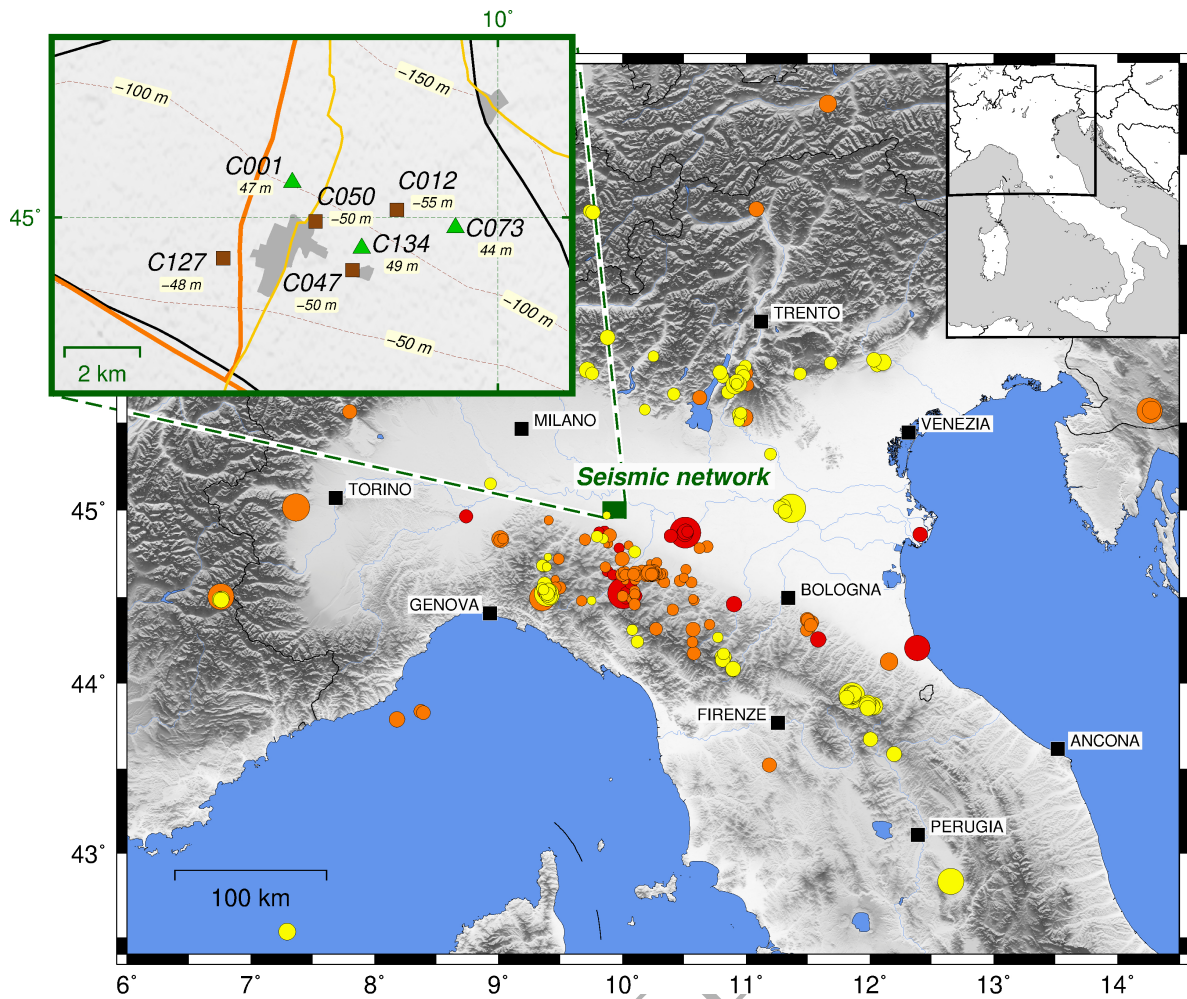


Figure 1. Study area and network configuration. Main panel: location of the microseismic network (dark green box) and epicenters of the selected earthquakes. Circles: earthquakes with $1.3 \leq M_L \leq 4.9$ (symbol dimensions are proportional to earthquake magnitude). Yellow, orange, and red symbols correspond to shallow ($h \leq 10$ km), intermediate ($10 \text{ km} < h \leq 25$ km) and deep ($h > 25$ km) events, respectively. Upper panel: microseismic network with location of surface and borehole instruments (green triangles and brown squares, respectively). The values shown under station labels indicate the instrument elevation with respect to sea level. Labelled dashed lines represent the isohypses of the Y-surface (see text). Main communication facilities of the area are also drawn (orange and yellow lines: highways and roads, respectively; black lines: railways).

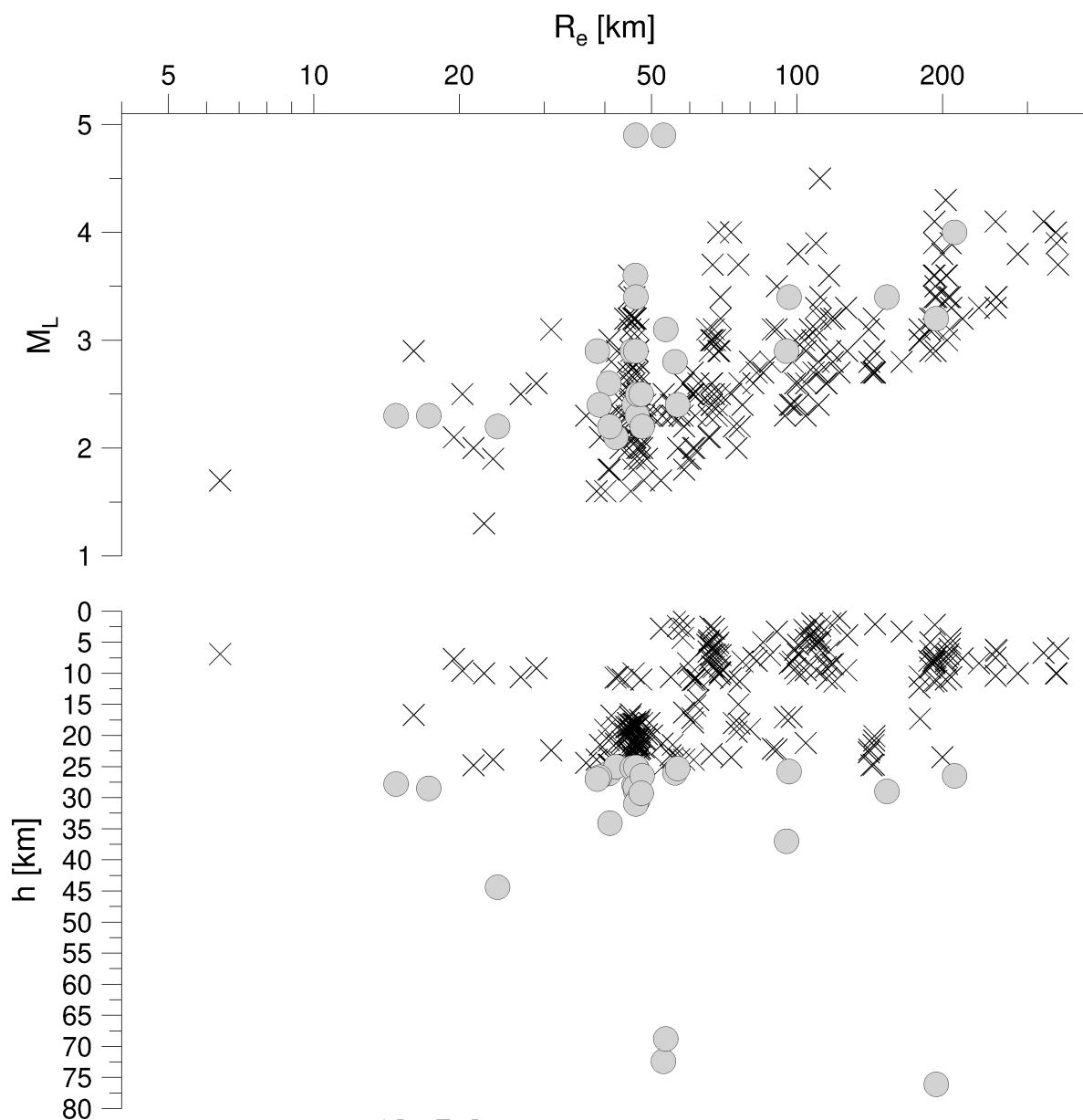


Figure 2. Upper graph: distribution of local magnitude with respect to epicentral distance of velocity data of selection 1 (crosses) and of velocity data of deep ($h > 25$ km) events (grey circles). Lower graph: as in the upper graph, but for the depth. Epicentral distance is measured from the center of the network.

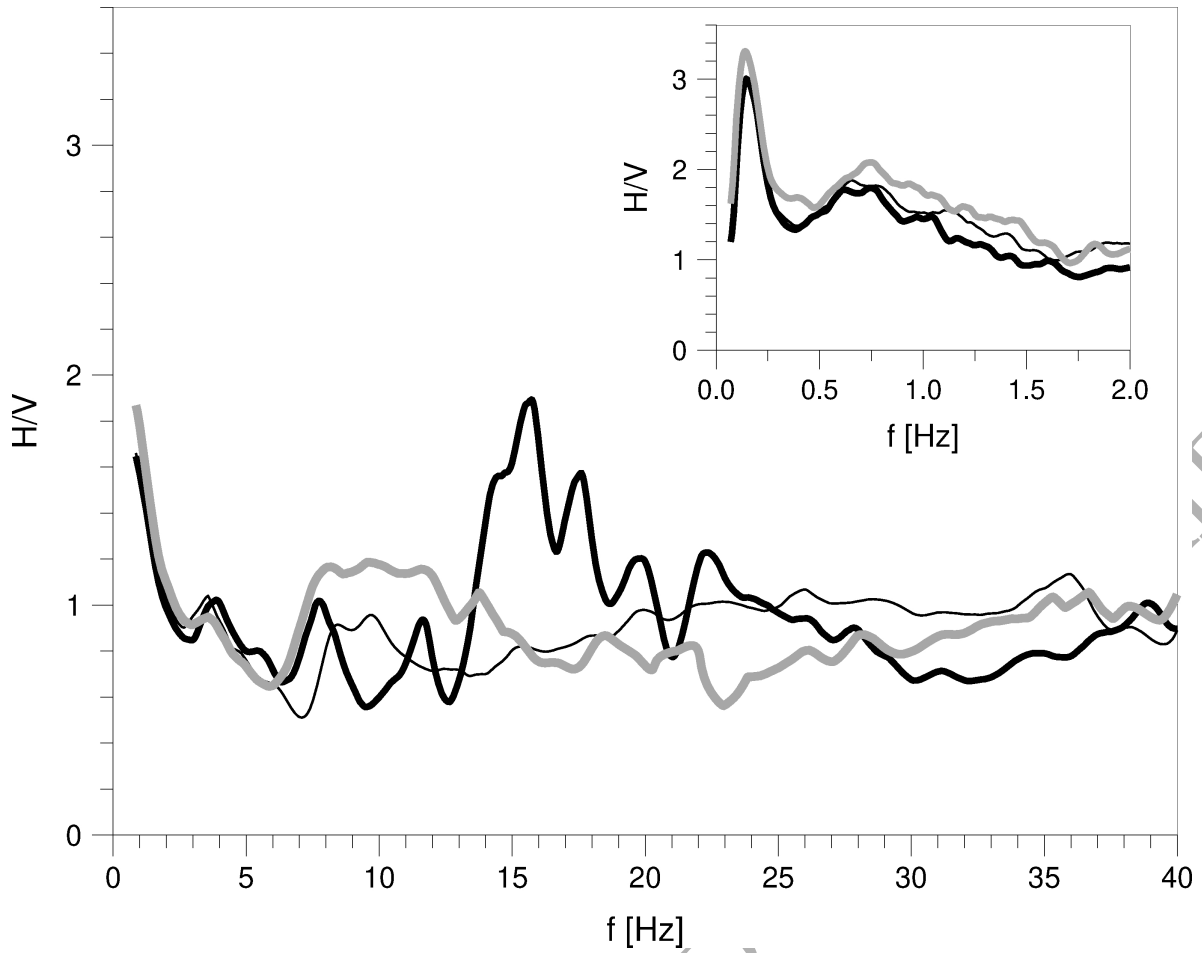


Figure 3. Horizontal-to-Vertical Spectral Ratios (HVSr) from microtremors recorded at surface stations: the inner panel shows a detail of the frequency range: 0-2 Hz. Thick black line: station C001; thin black line: station C073; grey line: station C134. Spectral ratios are computed using velocity data recorded in continuous mode.

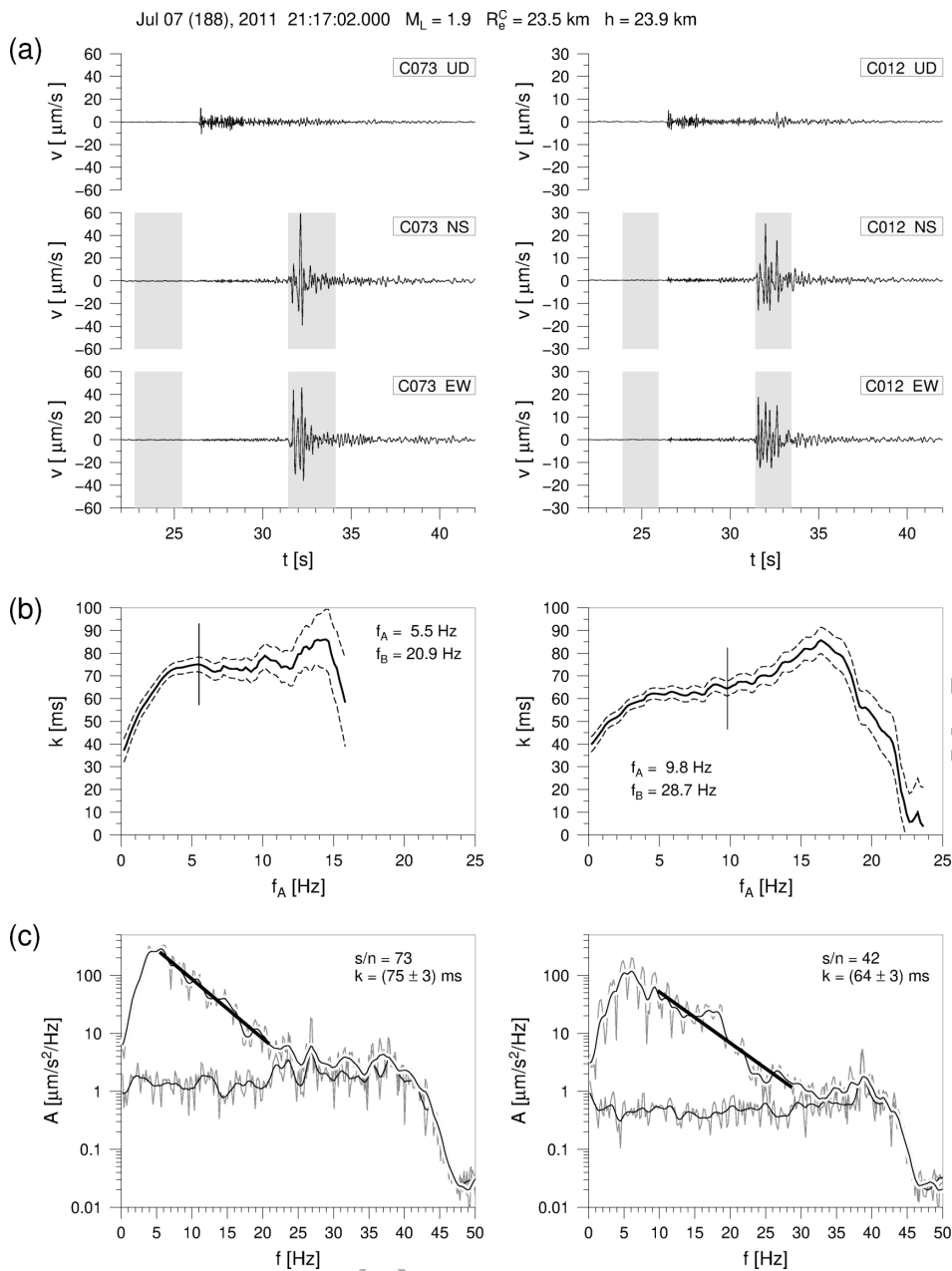


Figure 4. Example of k -record estimation: 7 July 2011 $M_L=1.9$ earthquake, recorded by stations C073 (surface) and C012 (borehole). R_e^C is the epicentral distance measured from the center of the network. h is depth. (a): velocity records (vertical, NS and EW components) and time windows used for noise and signal analysis (grey areas). (b): k -record estimates and standard deviations as a function of the lower limit of the frequency band adopted for the linear regression, f_A (solid and dashed lines, respectively). The adopted values of f_A and f_B are also indicated, and the vertical segment marks the chosen value of f_A . (c): signal and noise maximized acceleration spectra and linear regressions used to obtain the k -record estimate. Grey lines: original spectra of signal and noise; black thin line: smoothed noise spectrum; highlighted black thin line: smoothed signal spectrum; black thick line: linear regression. Signal-to-noise ratios, s/n , and k -record estimates are also indicated.

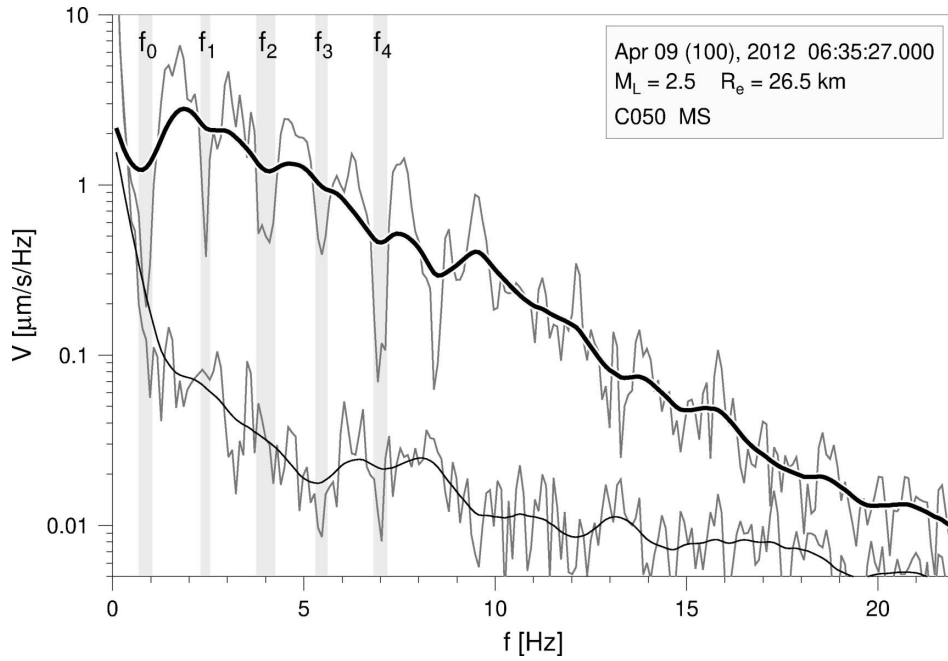


Figure 5. Example of interference frequencies estimation: 12 April 2012 $M_L=2.5$ earthquake, recorded at 26.5 km epicentral distance by station C050. Grey lines: original maximized velocity spectra of signal and noise; black thick and thin lines: smoothed maximized velocity spectrum of signal and noise, respectively; grey areas: measurement errors of the interference frequencies: f_N , $N = 0, 4$.

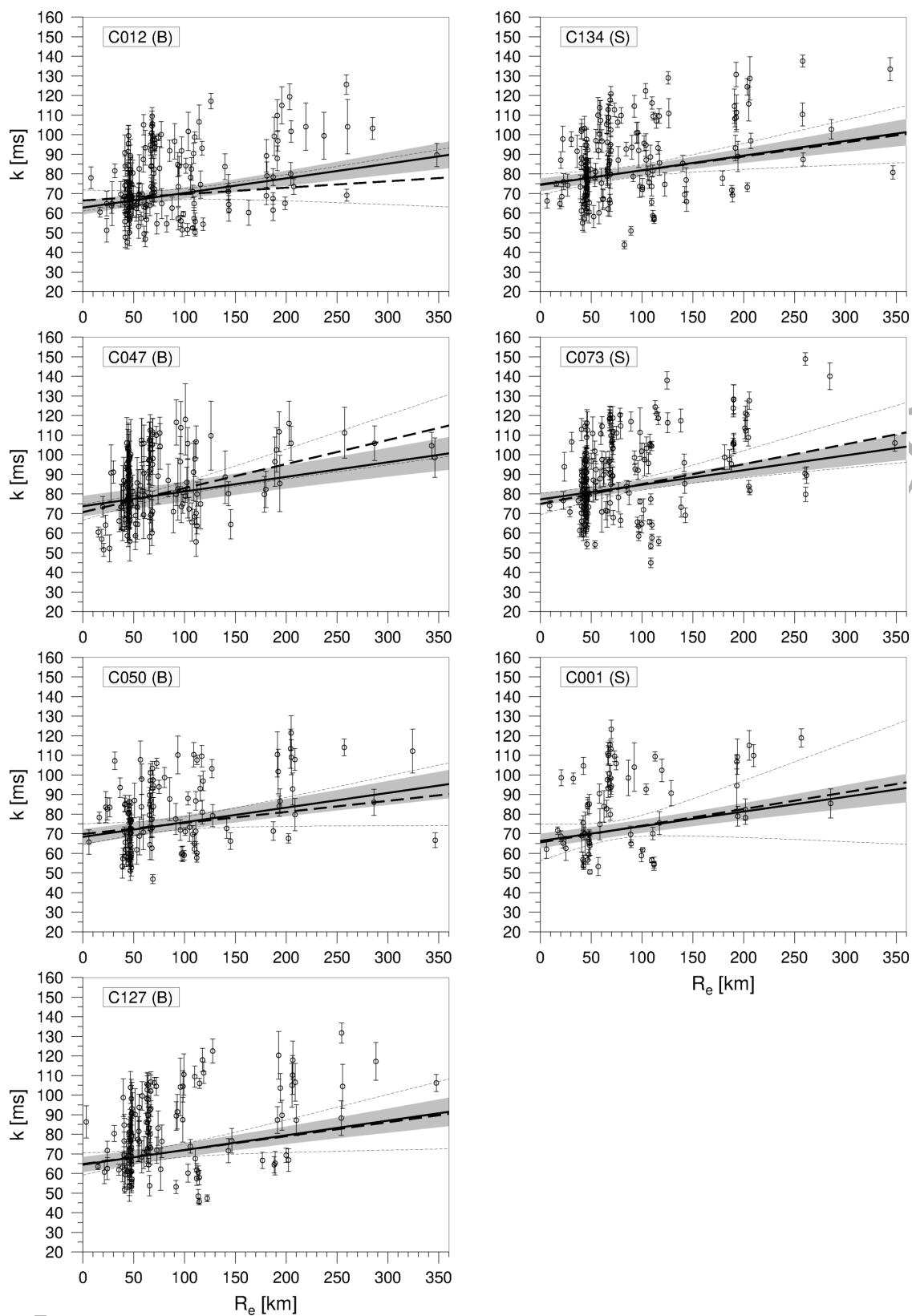


Figure 6. Functions $k(R_e)$ and corresponding 95% confidence limits, estimated with methods (A) (dashed lines) and (B) (solid line and grey area) for the 7 stations (S) of the microseismic network. Circles with error bars represent the k -record estimates.

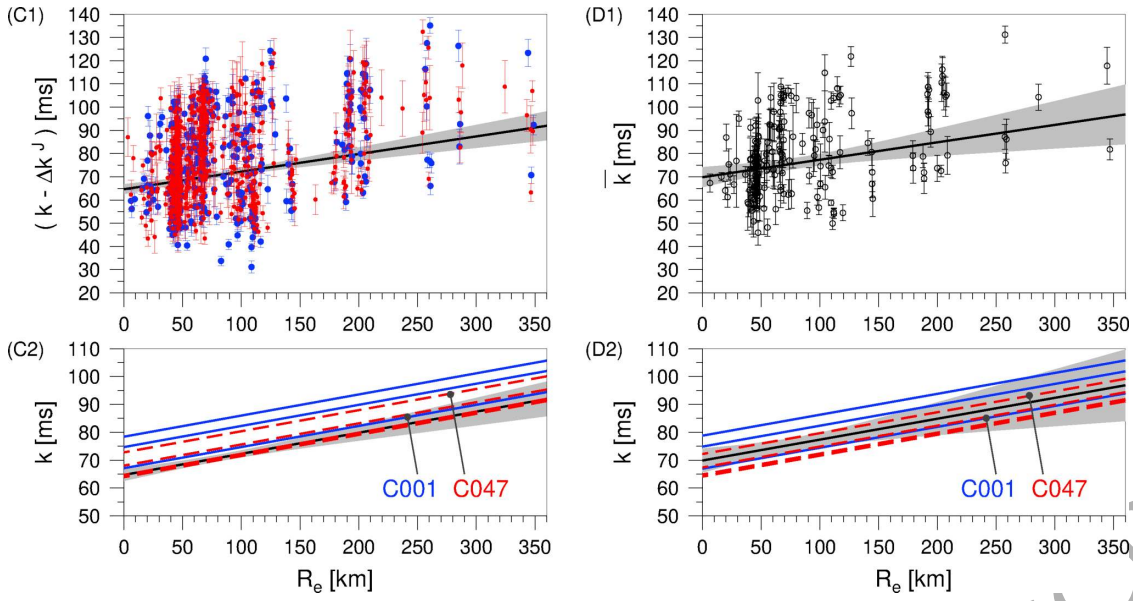


Figure 7. Left panels: method (C). Function $k(R_e)$ and corresponding 95% confidence limits estimated for the reference station C012 (black line and grey area, respectively). (C1): for each station J (blue: surface data; red: borehole data) circles with error bars represent the k -record minus Δk_{0100}^J values. (C2): blue and red lines represent the functions $k(R_e)$ obtained for surface and borehole stations, respectively; blue and red labels indicate the regression lines obtained for stations C001 and C047, respectively. Right panels: method (D). Function $k(R_e)$ and corresponding 95% confidence limits estimated for the average event k (black line and grey area, respectively). Epicentral distance is measured from the center of the network. (D1): circles with error bars represent the values of the average event k . (D2): blue and red lines represent the functions $k(R_e)$ obtained for surface and borehole stations, respectively; blue and red labels indicate the regression lines obtained for stations C001 and C047, respectively.

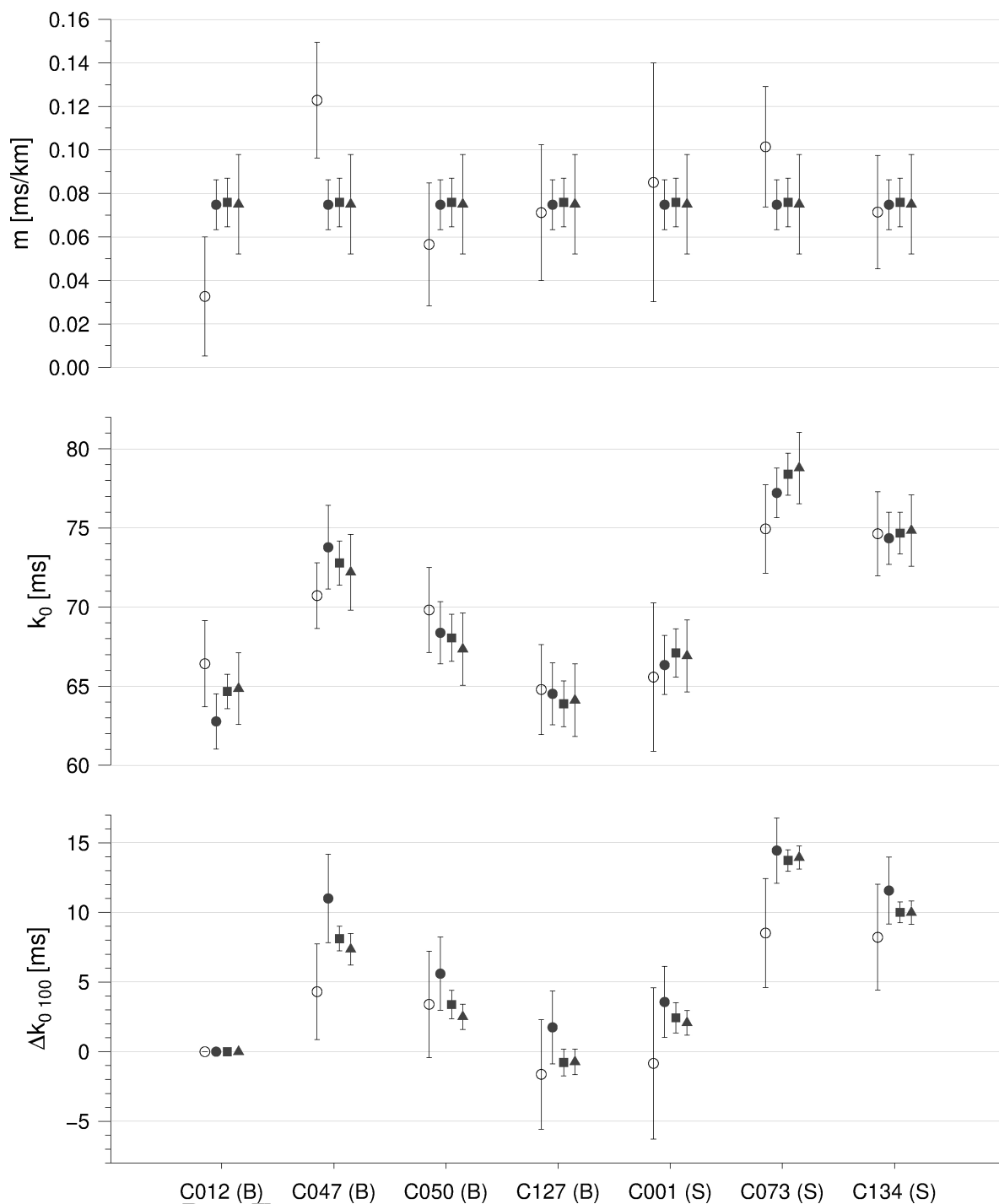


Figure 8. Upper panel: mean slope and corresponding ± 1 standard error of the linear regressions obtained for the 7 stations of the microseismic network with methods (A) (open circles), (B) (closed circles), (C) (squares) and (D) (triangles). Middle panel: as for the upper panel but for site-specific kappa. Lower panel: as for the upper panel but for the difference between the site-specific kappa estimated at each station and that of the reference station (C012).

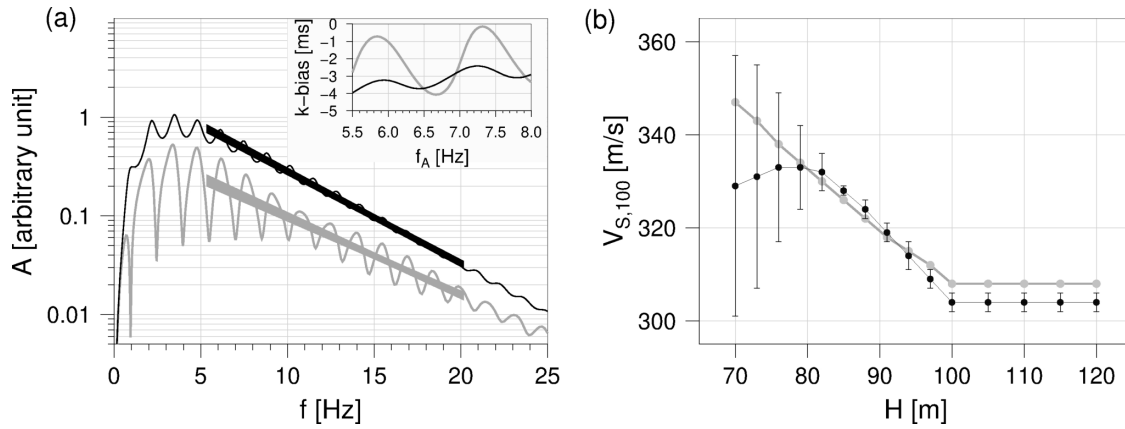


Figure 9. (a) estimation of k with stratigraphy characterized by wave velocity and quality factor gradually increasing with depth (see text for details). Main panel: surface acceleration spectrum and corresponding area enclosing the straight lines obtained from linear regressions with f_A ranging from 5.5 to 8.0 Hz and $f_B = 20$ Hz (black lines); borehole (100 m depth) acceleration spectrum and corresponding area enclosing the straight lines obtained from linear regressions with the same values of f_A and f_B (grey lines). The simulated acceleration spectra correspond to k values of 60 and 71 ms at 100 m depth and at surface, respectively (see text for details). Inset: k -bias corresponding to the linear regressions shown in the main panel. (b) estimation of $V_{S,100}$ for different values of bedrock depth (H) and stratigraphy characterized by wave velocity and quality factor gradually increasing with depth (see text for details). Grey symbols: simulated values; black symbols: values of $V_{S,100}$ and corresponding uncertainties, estimated with the method described in Section 4.4.

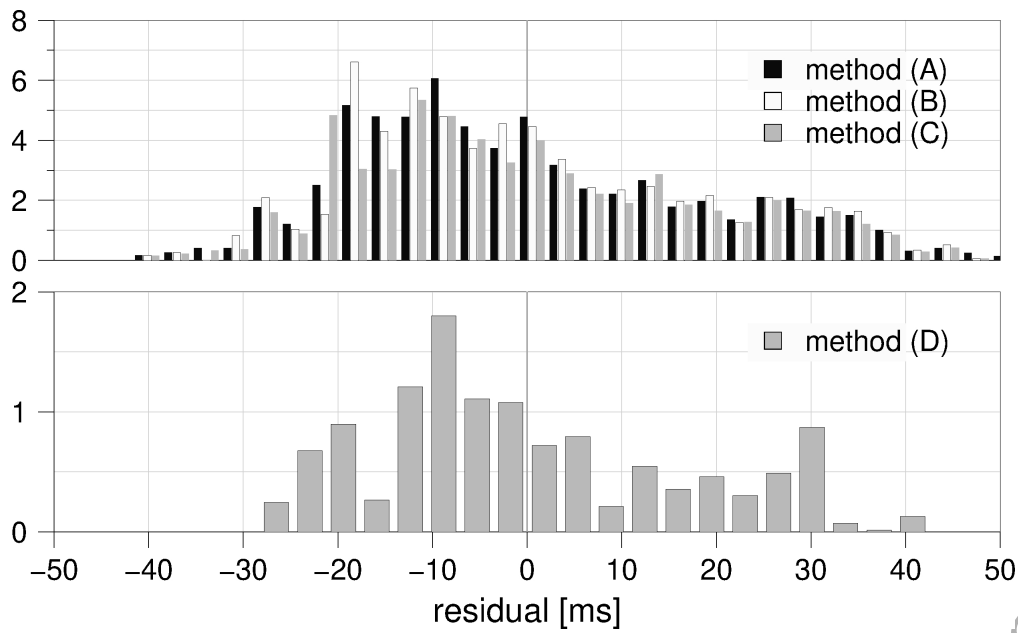


Figure 10. Distributions of the weighted residuals between observed and predicted k -record values obtained with the methods described in Section 4.3. Distributions are computed by considering the uncertainties of the k -record values (see Section 4.2).

ORIGINAL UNEDITED MANUSCRIPT

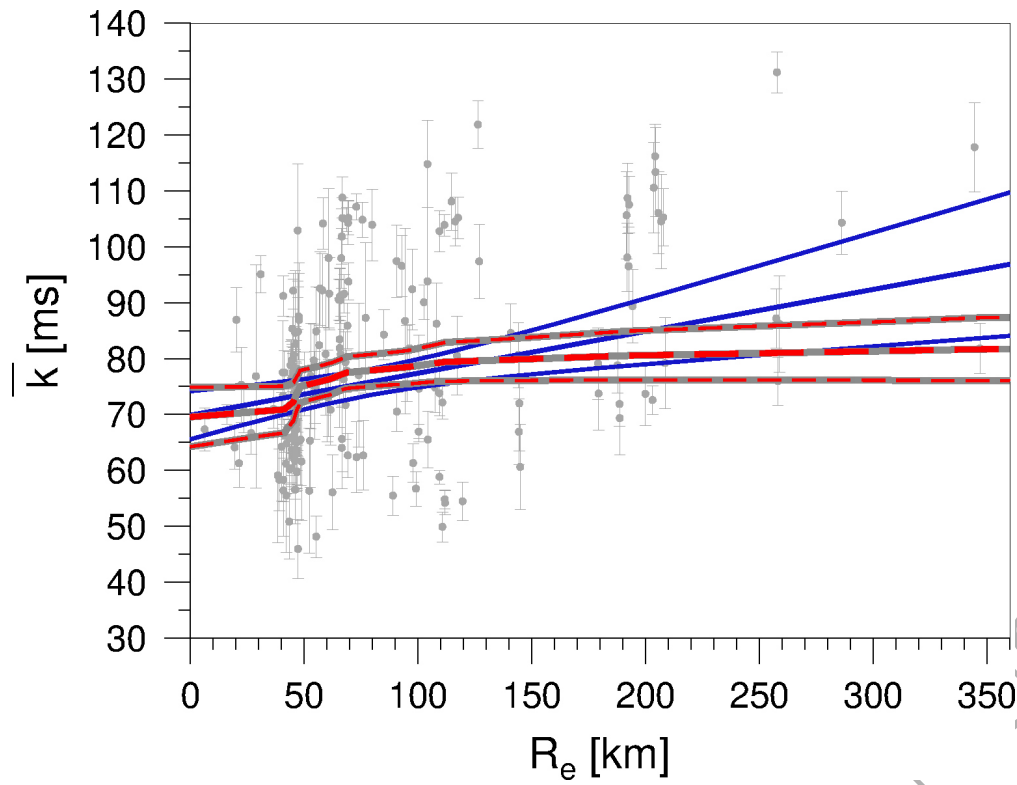


Figure 11. Function $k(R_e)$ and corresponding 95% confidence limits, estimated for the average event k with a non-parametric regression on epicentral distance (red lines) compared with the corresponding curves obtained with method (D) (blue lines). Circles with error bars represent the values of the average event k . Epicentral distance is measured from the center of the network.

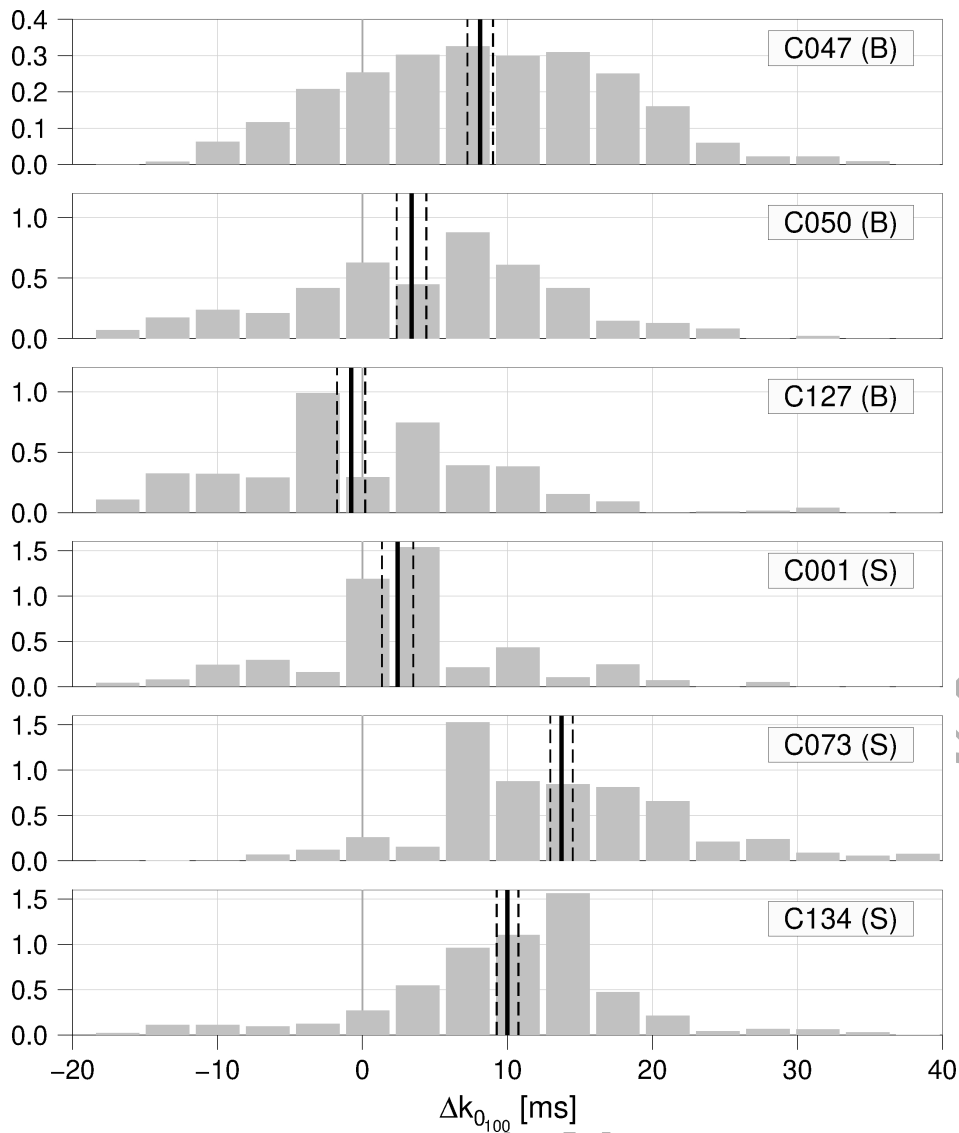


Figure 12. Distributions of Δk_{0100}^J obtained for stations: C001, C047, C050, C073, C127 and C134, using method (C). For each station, Δk_{0100}^J is referred to the station C012. Mean values and corresponding standard error intervals are also indicated (vertical black lines).

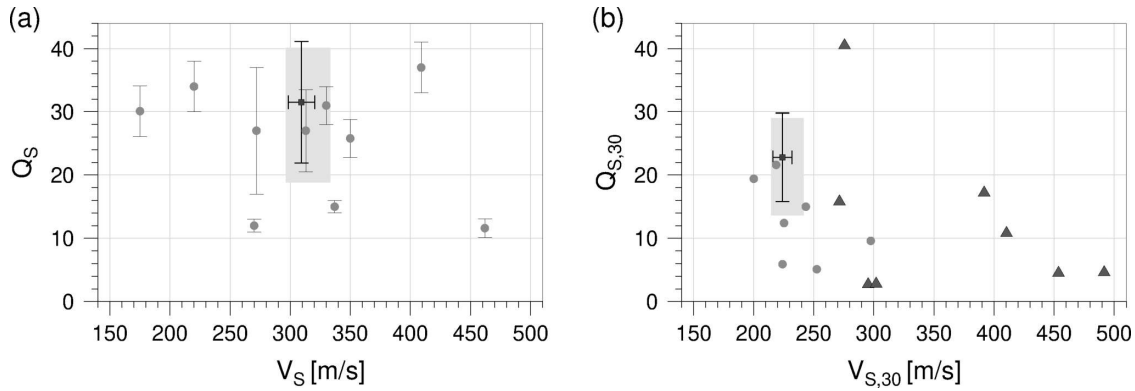


Figure 13. (a) Time-averaged S-wave velocity and quality factor at 100 m depth computed in this work, compared with the estimates of Boore et al. (2020). Black symbol with error bars: values of $V_{S,100}$ and $Q_{S,100}$ obtained with method A1; grey area: values of $V_{S,100}$ and $Q_{S,100}$ obtained with method A2; grey symbols with error bars: S-wave velocities and quality factors averaged over a depth range from about 8 to 70 m, estimated by Boore et al. (2020) with borehole data collected in the San Francisco Bay area and in the San Fernando Valley characterized by fine- to medium-grained lithologies. (b) Time-averaged S-wave velocity and quality factor at 30 m depth computed in this work, compared with the estimates of the same parameters obtained by Boxberger et al. (2017). Black symbol with error bars: values of $V_{S,30}$ and $Q_{S,30}$ obtained with method A1; grey area: values of $V_{S,30}$ and $Q_{S,30}$ obtained with method A2; grey circles and black triangles: values of $V_{S,30}$ and $Q_{S,30}$ obtained by Boxberger et al. (2017) with data collected in Europe and Central Asia characterized by clayey and sandy lithologies, respectively.

Table 1. Seismic station characteristics.

Station	Lat. (°N)	Lon. (°E)	Elev. ^a (m)	Depth ^b (m)	Digitizer	Sensor
C001	45.00833	9.93088	47	0	Lennartz M24/NET	LE-3Dlite MkII
C012	45.00178	9.96603	45	100	Lennartz M24/NET	LE-3D/BH
C047	44.98742	9.95107	50	100	Lennartz M24/NET	LE-3D/BH
C050	44.99900	9.93869	50	100	Lennartz M24/NET	LE-3Dlite MkII
C073	44.99751	9.98572	44	0	Lennartz M24/NET	LE-3D/BH
C127	44.99029	9.90762	52	100	Lennartz M24/NET	LE-3D/BH
C134	44.99266	9.95421	49	0	Lennartz M24/NET	LE-3Dlite MkII

^a Above sea level.^b Below ground level.**Table 2.** Percentiles, p , of parameter distributions used to estimate k -record: time window duration, T_d ; frequency limits of the least square regression, f_A and f_B ; frequency bandwidth of the least square regression, $f_B - f_A$; difference between the first limit of the least square regression, f_A , and the corner frequency of the event, f_c , estimated through an appropriate scaling with the local magnitude (see text); signal-to-noise ratio, s/n .

p	T_d (s)	f_A (Hz)	f_B (Hz)	$f_B - f_A$ (Hz)	$f_A - f_c$ (Hz)	s/n ^a
5	3.5	2.0	9.8	6.5	-1.4	3.3
20	4.8	3.1	12.5	8.0	-0.3	4.5
35	5.5	4.3	13.6	9.0	0.4	5.8
50	6.3	4.6	15.3	10.2	1.2	7.4
65	7.7	5.7	17.3	11.6	1.9	10.5
80	9.3	7.1	19.2	13.5	3.3	17.6
95	12.3	9.6	24.2	17.7	5.9	59.5

^a Given the acceleration MS of signal and noise, $S(f)$ and $N(f)$ respectively, s/n is defined as:

$$\frac{s}{n} = \sqrt{\frac{\int_{f_A}^{f_B} S(f)^2 df}{\int_{f_A}^{f_B} N(f)^2 df}} \quad (16)$$

Table 3. Slope of the linear trend of k with epicentral distance (m), site-specific kappa (k_0) and difference between the site-specific kappa estimated at each station and that of the reference station (Δk_{0100}) obtained with methods (A), (B), (C) and (D) for the stations of the microseismic network. σ_m ; σ_{k_0} and $\sigma_{\Delta k_{0100}}$ are the standard errors of m , k_0 and Δk_{0100} , respectively. e_k is the root-mean-squared error of the regression. N_k and $N_{\Delta k}$ are the number of data employed to estimate the parameters of $k(R_e)$ and Δk_{0100} , respectively. An asterisk next to the method label indicates that k -record estimates of stations C001 and C047 have been excluded from the computation of the parameters reported in the table.

Station	M	N_k	m (ms/km)	σ_m (ms/km)	k_0 (ms)	σ_{k_0} (ms)	e_k (ms)	$N_{\Delta k}$	Δk_{0100} (ms)	$\sigma_{\Delta k_{0100}}$ (ms)
C012 (B)	(A)	159	0.03	0.03	66	3	4	159	0	-
	(B)	159	0.07	0.01	63	2	5	159	0	-
	(B)*	159	0.07	0.01	63	2	5	159	0	-
	(C)	159	0.08	0.01	65	1	5	165	0	-
	(C)*	159	0.07	0.01	65	1	5	164	0	-
	(D)	-	0.08	0.02	65	2	4	165	0	-
	(D)*	-	0.07	0.02	65	2	4	164	0	-
C047 (B)	(A)	145	0.12	0.03	71	2	2	145	4	3
	(B)	145	0.07	0.01	74	3	5	145	11	3
	(C)	145	0.08	0.01	73	1	5	114	8	1
	(D)	-	0.08	0.02	72	2	4	149	7	1
C050 (B)	(A)	113	0.06	0.03	70	3	4	113	3	4
	(B)	113	0.07	0.01	68	2	5	113	6	3
	(B)*	113	0.07	0.01	69	2	5	113	6	3
	(C)	113	0.08	0.01	68	1	5	111	3	1
	(C)*	113	0.07	0.01	68	2	5	111	3	1
	(D)	-	0.08	0.02	67	2	4	130	2	1
	(D)*	-	0.07	0.02	68	2	4	129	3	1
C127 (B)	(A)	127	0.07	0.03	65	3	4	127	-2	4
	(B)	127	0.07	0.01	65	2	5	127	2	3
	(B)*	127	0.07	0.01	65	2	5	127	2	3
	(C)	127	0.08	0.01	64	1	5	120	-1	1
	(C)*	127	0.07	0.01	64	2	5	120	-1	1
	(D)	-	0.08	0.02	64	2	4	142	-1	1
	(D)*	-	0.07	0.02	64	2	4	140	-1	1
C001 (S)	(A)	70	0.09	0.05	66	5	7	70	-1	5
	(B)	70	0.07	0.01	66	2	5	70	4	3
	(C)	70	0.08	0.01	67	2	5	72	2	1
	(D)	-	0.08	0.02	67	2	4	84	2	1
C073 (S)	(A)	173	0.10	0.03	75	3	6	173	9	4
	(B)	173	0.07	0.01	77	2	5	173	14	2
	(B)*	173	0.07	0.01	77	2	5	173	14	2
	(C)	173	0.08	0.01	78	1	5	141	14	1
	(C)*	173	0.07	0.01	78	1	5	141	14	1
	(D)	-	0.08	0.02	79	2	4	175	14	1
	(D)*	-	0.07	0.02	79	2	4	169	14	1
C134 (S)	(A)	154	0.07	0.03	75	3	5	154	8	4
	(B)	154	0.07	0.01	74	2	5	154	12	2
	(B)*	154	0.07	0.01	75	2	5	154	12	3
	(C)	154	0.08	0.01	75	1	5	132	10	1
	(C)*	154	0.07	0.01	75	1	5	132	10	1
	(D)	-	0.08	0.02	75	2	4	165	10	1
	(D)*	-	0.07	0.02	75	2	4	155	10	1

Table 4. Differences between adjacent interference frequencies and time-averaged S-wave velocity of the uppermost 100 m estimated with the borehole stations. The differences $\Delta f_{N,N+1}$ estimated with frequencies f_N ($N = 0, 4$); the corresponding weighted mean, Δf , and the corresponding time-averaged S-wave velocity, $V_{S,100}$, are reported. $\sigma_{\Delta f_{N,N+1}}$, $\sigma_{\Delta f}$ and $\sigma_{V_{S,100}}$ are the standard errors. M_N is the number of data used to compute f_N .

Stat.	M_0	$\Delta f_{0,1}$	$\sigma_{\Delta f_{0,1}}$	M_1	$\Delta f_{1,2}$	$\sigma_{\Delta f_{1,2}}$	M_2	$\Delta f_{2,3}$	$\sigma_{\Delta f_{2,3}}$	M_3	$\Delta f_{3,4}$	$\sigma_{\Delta f_{3,4}}$	M_4	Δf	$\sigma_{\Delta f}$	$V_{S,100}$	$\sigma_{V_{S,100}}$
		(Hz)	(Hz)		(Hz)	(Hz)		(Hz)	(Hz)		(Hz)	(Hz)		(Hz)	(Hz)	(m/s)	(m/s)
C012	50	1.48	0.04	49	1.54	0.05	38	1.53	0.06	28	1.56	0.08	18	1.52	0.03	303	7
C047	34	1.43	0.05	24	1.47	0.06	20	1.52	0.08	14	-	-	-	1.46	0.04	291	8
C050	38	1.55	0.05	37	1.54	0.05	38	1.45	0.06	26	1.58	0.08	21	1.53	0.03	305	7
C127	35	1.61	0.06	37	1.55	0.06	37	1.69	0.08	21	1.77	0.12	14	1.62	0.04	325	9

Table 5. Site specific parameters referring to the installation area of the network, estimated with methods A1, A2 and A3 (see text): difference between the values of k estimated at the surface and at the boreholes depth ($\Delta k_{0,100}$); time-averaged S-wave velocity and quality factor of the uppermost 100 m ($V_{S,100}$ and $Q_{S,100}$, respectively); time-averaged S-wave velocity and quality factor of the uppermost 30 m ($V_{S,30}$ and $Q_{S,30}$, respectively). For methods A1 and A3, the results are expressed in terms of mean value and standard deviation, for method A2 in terms of minimum and maximum values.

	method A1	method A2	method A3
$\Delta k_{0,100}$ (ms)	11 ± 3	11 ± 3	11 ± 3
$V_{S,100}$ (m/s)	309 ± 11	296 ; 333	309 ± 11
$Q_{S,100}$	31 ± 10	19 ; 40	28 ± 9
$V_{S,30}$ (m/s)	224 ± 8	215 ; 241	—
$Q_{S,30}$	23 ± 7	14 ; 29	—